UNIVERSITY OF CALIFORNIA SAN DIEGO

Application of Micro-, Surface Enhanced, and Tip Enhanced Raman Spectroscopy for Thermography and Damage Analysis of Heat Assisted Magnetic Recording Systems

A Thesis submitted in partial satisfaction of the requirements for the degree of Master of Science

in

Engineering Sciences (Mechanical Engineering)

By

Benjamin Ying-Xiu Suen

Committee in Charge:

Professor Frank E. Talke, Chair
Professor Vlado A. Lubarda
Professor Marc A. Meyers

2019

The Thesis of Benjamin Ying-Xiu Suen is approved, and is acceptable in quality and form for publication on microfilm and electronically:

Chair

University of California San Diego

2019

DEDICATION

To my parents Chi-Yeung John and Annie Suen and my brother Jonathan Suen

TABLE OF CONTENTS

LIST OF ABBREVIATIONS

LIST OF FIGURES

LIST OF TABLES

ACKNOWLEDGEMENTS

Foremost, I would like to express my gratitude and sincere appreciation to my advisor Professor Frank E. Talke for his support throughout my research work and throughout my graduate and undergraduate studies. Professor Talke's advice, encouragement, and unwavering support enabled me to investigate scientific subjects across a broad range of fields. He has inspired me to explore the frontiers of science and engineering.

I would also like to express my gratefulness towards Professor Vlado Lubarda for all the advice and support that he has given me throughout my academic studies. Professor Vlado Lubarda provided me with countless amounts of valuable advice.

Additionally, I would like to acknowledge Longqiu Li for helping me with the Raman thermometry experiments. I would like to acknowledge Andreas Rosenkranz for helping me with the experiments on the TERS setup with the Innova-IRIS AFM and conducting measurements of my samples using the Nanonics TERS setup. I would like to acknowledge Lindsay Freeman for conducting measurement of my samples using the Nanonics TERS setup. I would like to acknowledge Professor Yeshaiahu Fainman for letting us use his Nanonics TERS setup. I would like to acknowledge Professor Andrea Tao for letting us use her Innova-IRIS TERS setup. I would like to acknowledge Tyler Dill and Darwin Zwissler for helping with the Innova-IRIS TERS setup and the SERS experiments. I would like to acknowledge Andrew King for providing technical support on both Renishaw Raman spectrometers. I would like to acknowledge Ray Descoteaux for machining parts for the experiment and providing technical support. I would like to acknowledge Frederick E. Spada for providing support on various aspects of the

experiments. I would like to acknowledge Octavio Ochoa, Marina Robenko, and Iris Villanueva for providing administrative support.

Finally, I would like to thank my parents Chi-Yeung John Suen and Annie Suen and my brother Jonathan Suen for their support thought my time at UCSD. I would also like to thank my lab mates Pierre Freneau, Youyi Fu, Oren Gotlib, Kevin Joslin, Matthew Kohanfars, Marina Krijgsman, Siu Lim Lee, Yu Li, Liane Matthes, Karcher Morris, Alex Phan, Christoph Schade, Young Woo Seo, Ella Stimpson, Tan Trinh, Dora Trieu, Buu Truong, Phuong Truong, Nick Williams, and Quin Zhao for all the support and companionship during my time in the lab.

VITA

Education

2012 Bachelor of Science, University of California San Diego

2019 Master of Science, University of California San Diego

Publications

Gauvin, M., Zheng, H., Suen, B., Lee, J., Kang, H. J., & Talke, F. E. "Enhanced photo-thermal stability of modified PFPE lubricants under laser beam exposure." *IEEE Transactions on Magnetics* 47.7 (2011): 1849-1854.

Li, L., Suen, B., Seo, Y., King, A., & Talke, F. E. "TuA-2-1 A NEW TEST EXPERIMENTAL SET-UP FOR STUDING THE HEAD/DISK INTERFACE IN HEAT ASSISTED MAGNETIC RECORDING USING TIP-ENHANCED RAMAN SPECTROSCOPY." *Proceedings of JSME-IIP/ASME-ISPS Joint Conference on Micromechatronics for Information and Precision Equipment: IIP/ISPS joint MIPE 2015*. The Japan Society of Mechanical Engineers, 2015.

Li, Longqiu, Benjamin Suen, and Frank E. Talke. "Investigation of Temperature Dependence of Raman Shift of Diamond-Like Carbon Coatings Used in Heat-Assisted Magnetic Recording." *IEEE Transactions on Magnetics* 51.11 (2015): 1-4.

Li, Longqiu, Kaipeng Liu, Benjamin Suen, Qingkang Liu, Andrew King, and Frank E. Talke. "Numerical and experimental study of near-field heating using tip-enhanced Raman spectroscopy (TERS)." *Tribology Letters* 66.1 (2018): 26.

Rosenkranz, A., Freeman, L., Suen, B., Fainman, Y., & Talke, F. E. "Tip-Enhanced Raman Spectroscopy Studies on Amorphous Carbon Films and Carbon Overcoats in Commercial Hard Disk Drives." *Tribology Letters* 66.2 (2018): 54.

Phan, A., Truong, P., Camp, A., Stewart, K., Suen, B., Weinreb, R. N., & Talke, F. E. "A Wireless Handheld Pressure Measurement System for in vivo Monitoring of Intraocular Pressure in Rabbits." *IEEE Transactions on Biomedical Engineering* (2019).

Field of Study

Major Field: Engineering Sciences (Mechanical Engineering)

Studies in material sciences and design

Professor Frank E. Talke

ABSTRACT OF THE THESIS

Application of Micro-, Surface Enhanced, and Tip Enhanced Raman Spectroscopy for Thermography and Damage Analysis of Heat Assisted Magnetic Recording Systems

by

Benjamin Ying-Xiu Suen

Master of Science in Engineering Sciences (Mechanical Engineering)

University of California San Diego, 2019

Professor Frank E. Talke, Chair

This thesis presents a method that provides important insights into the nanoscale photo-thermal damage process, thus allowing engineers to better find solutions to abate the wear process. With the ever-increasing need for data storage, new technologies that increase the storage capacity of computer memory are necessary for the advancement of computational systems. One such technology is heat assisted magnetic recording (HAMR) for hard disk drives. Heat-assisted magnetic recording has the promise of offering a cost-effective way of increasing the data storage density of computer disk

drives used for the bulk storage of data. While HAMR technology has seen promising advancements towards widespread deployment, engineering challenges remain due to the fact that HAMR drives degrade and fail due to nanoscale photo-thermal wear.

In this thesis, tip enhanced Raman spectroscopy is used to generate near-field radiation, similar to that which causes the nanoscale photo-thermal wear in HAMR drives, while simultaneously measuring the material properties of a sample which is exposed to said radiation. The method presented in this thesis is intended to be used in conjunction with numerical models, other supporting experimentation, and component-level testing in order to better predict the wear life of HAMR drives.

It was found that it is possible to generate near-field radiation using tip enhanced Raman spectroscopy on a sample of hard disk drive media while simultaneously measuring chemical properties *in situ*. Further work will have to be conducted in order to generate intense enough radiation to clearly damage the hard disk drive media and to map the damage caused by the radiation.

1. Introduction

Modern computer technology has permeated into many aspects of society and has provided numerous benefits to a wide range of people. It is predicted that the growth and adaptation of computer technologies will continue and allow for the quality of life for many individuals to continuously improve. However, with the growth of computerization, the need for data storage will grow. Industry forecasts predict that data generation will grow over four times in the period from 2016 to 2020 due to technologies such as the internet of things, big data analytics, mobility, and cloud computing [1]. A graph showing the predicted growth in data storage, from Seagate Technology and IDC, is shown in Figure 1 below.

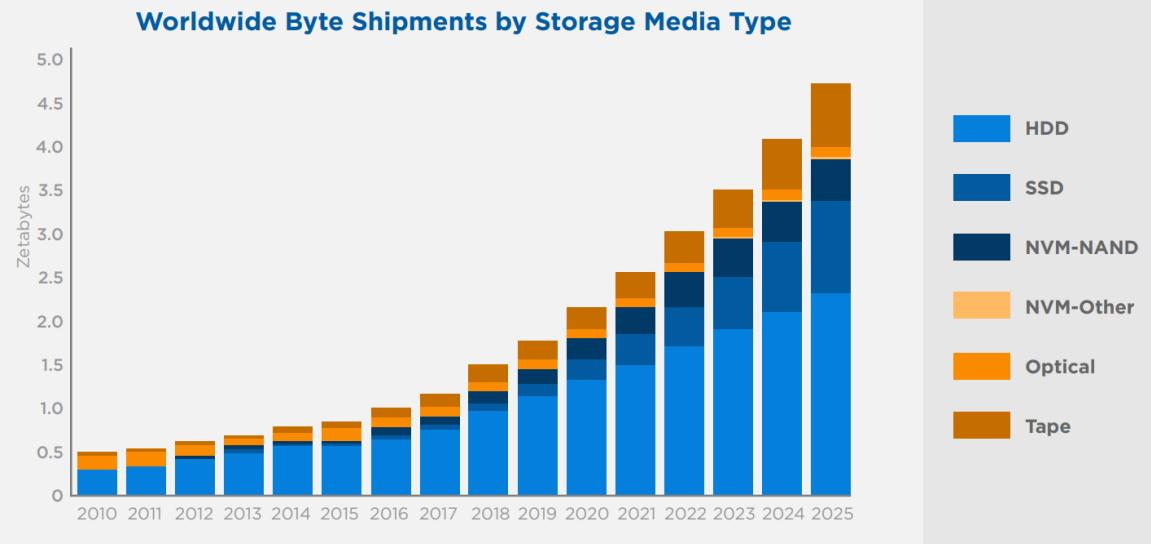

Figure 1: Predicted growth in data storage devices by Seagate Technology and IDC [2].

Although the need for increased data storage capacity will probably be partially met by improvements in solid state drive technologies, hard disk drives will most likely

have a significant role in providing future bulk data storage due to lower cost per byte of data stored [1]. In order for hard disk drives to remain a viable alternative or complement to solid state drive technology in the future data storage market, the technology must improve in terms of storage density and cost per byte of data stored.

1.1. Heat Assisted Magnetic Recording

A promising improvement to hard disk drives is the use of heat assisted magnetic recording (HAMR). HAMR allows for hard disk drives to improve their storage capacity by improving the areal density of the data stored within the hard disk media. It is predicted that HAMR technology can increase the areal density of hard disk drives by 15 to 30 percent compounded annual growth rate [3]. Additionally, HAMR technology is predicted to increase areal density from 1 terabyte per square inch to 5-10 terabytes per square inch when combined with bit patterned media [1].

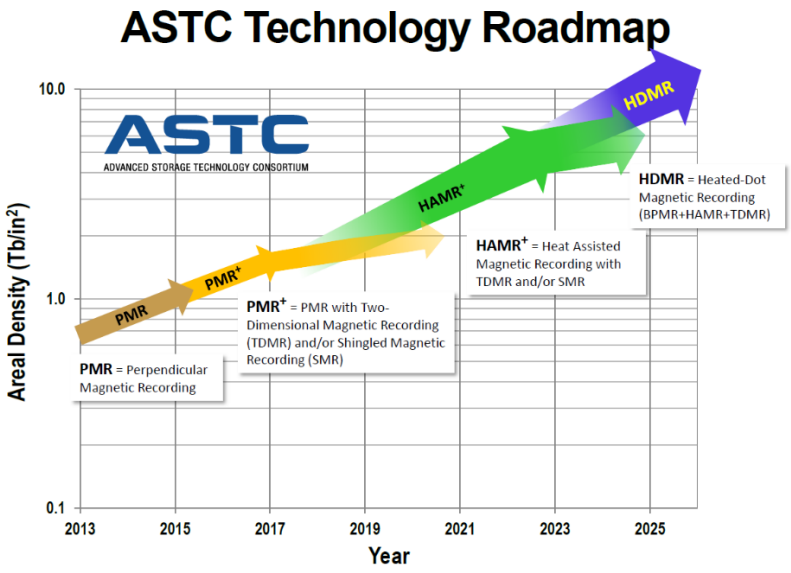

Figure 2: Predicted growth in areal density from various hard disk drive technologies [4].

A figure illustrating Advanced Storage Technology Consortium's forecast of areal density growth can be seen in Figure 2 above.

Heat Assisted Magnetic Recording (HAMR) is a technology that can increase areal density by overcoming the magnetic recording trilemma that hinders areal density growth in current hard disk drives. One part of the trilemma is that if one desires to use magnetic recording media with smaller magnetic domains, and thereby increasing signal to noise ratio and areal density, one must use media with high magnetic anisotropy to prevent bits from randomly shifting magnetic orientations due to the superparamagnetic effect. When one uses a highly anisotropic recording media, it also exhibits high magnetic hardness, which makes the media hard or impossible to be written by a flying magnetic head [5]. HAMR overcomes this trilemma by exploiting material properties at the Curie temperature that allow for writing of data on recording media that exhibits high magnetic anisotropy at room temperature.

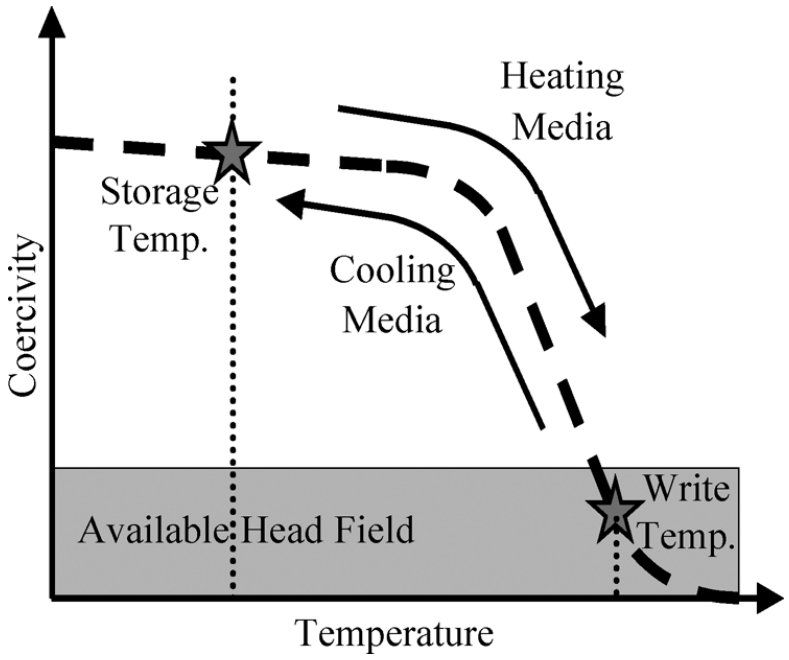

Figure 3: The thermal process of heat assisted magnetic recording technology [6].

HAMR technology operates in a similar fashion as a current hard disk drive except the read/write apparatus can heat the magnetic media to approximately its Curie temperature during the write process. In HAMR the write process begins when a pulsed laser is used to heat a spot on the recording media to approximately its Curie temperature. As the recording media approaches its Curie temperature it starts to exhibit paramagnetic properties and becomes susceptible weaker to magnetic fields. A magnetic field, in the direction corresponding to the data bit being written, is then applied by the write coil to magnetize the heated spot. The magnetic bit is recorded as the spot cools after the laser radiation pulse has ended [6]. A diagram of this thermos-magnetic process can be seen in Figure 3 above, and a diagram comparing the HAMR write mechanism to a conventional perpendicular magnetic recording write mechanism can be seen in Figure 4 below.

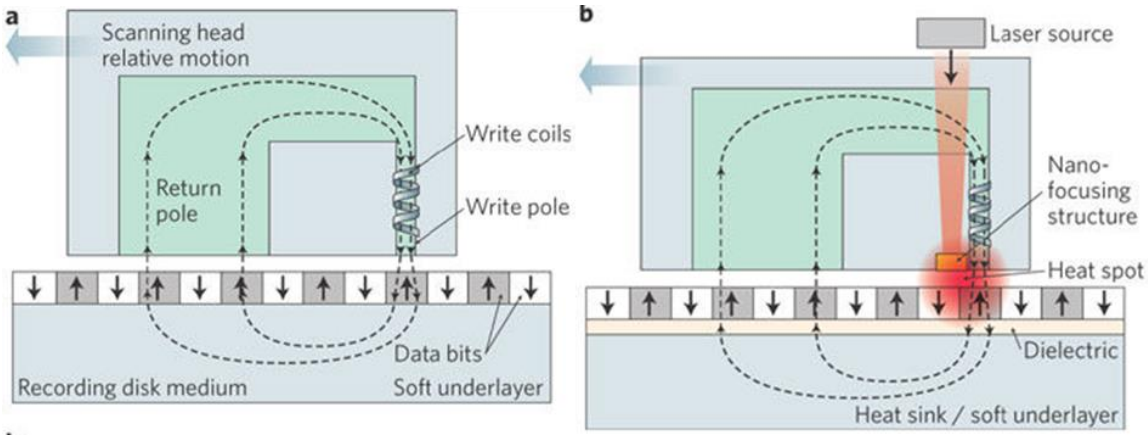

Figure 4: A conventional perpendicular magnetic recording write mechanism (a) versus a heat assisted magnetic recording write mechanism (b) [7].

Although HAMR is a promising technology, it faces a number of engineering challenges. A major concern is that the repetitive cycling of high temperatures and extreme electromagnetic flux may cause media degradation and the premature failure of the HAMR drive. Additionally, for the HAMR process to record data at higher bitrates

and areal densities as compared to current drives, the entire process must occur rapidly and in nanoscale dimensions. The nanoscopic scales make measurement of the degradation processes occurring in the drive difficult. A potential way to measure important parameters of the HAMR wear process is through the use of Raman spectroscopy.

1.2. Raman Spectroscopy

Raman spectroscopy is a rotational-vibrational spectroscopy method used to measure various aspects of molecules, particles, or bulk materials. In essence, Raman spectroscopy measures the electronic state of molecules by measuring the molecule's vibrational response to an electromagnetic field in the infrared to ultraviolet wavelengths. When a molecule is exposed to electromagnetic radiation such as from a laser beam, photos will interact with the molecule's electron cloud and some will inelastically scatter at a different wavelength than its original state. This is referred to as Raman scattering [8].

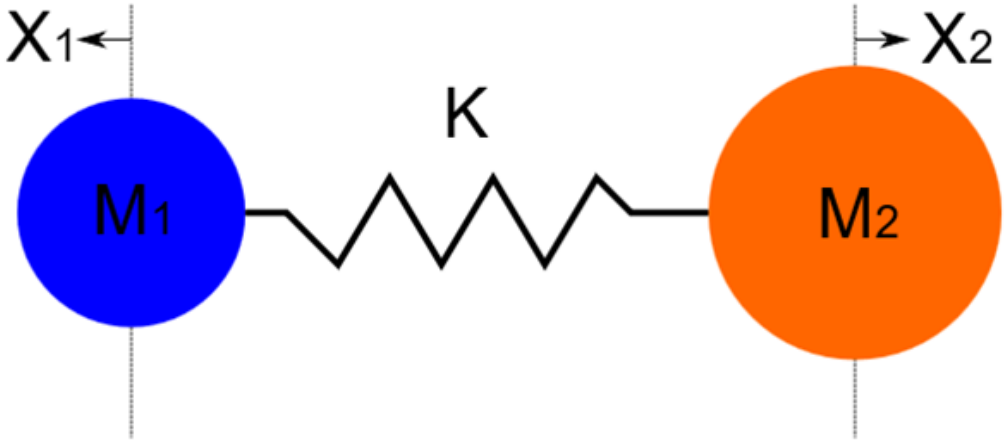

Figure 5: Simplified spring-mass model of a diatomic molecule adapted from [9].

In order to understand the phenomena of Raman scattering, one has to first understand the vibrational properties of molecules. One can use a simplified molecule, such as the one in Figure 5, above, in order to obtain a fundamental understanding of molecular vibrations. In the above figure, there are two atoms with masses m_1 and m_2 and a bond between the two atoms with spring constant K. When vibrating, the atoms exhibit displacements x_1 and x_2 from their equilibrium position. The coordinate system is measured from the point of view of the center of gravity of the two atoms at their equilibrium state; no rigid body translation is exhibited. Using Newton's second law, we can readily derive the equation of motion for the displacement between the two molecules, seen in Equation 1 below, where q_0 is the maximum displacement, φ is the phase constant, and t is time. The following derivations and equations in this subsection are adapted from references [8] and [9].

Equation 1: $$q = q_0 \sin(2\pi \nu_m t + \varphi)$$

ν_m is the natural frequency as defined in Equation 2 below.

Equation 2: $$\nu_m = \frac{1}{2\pi}\sqrt{\frac{K}{\mu}}$$

μ is the reduced mass as defined by Equation 3 below.

Equation 3: $$\mu = \frac{m_1 m_2}{m_1 + m_2}$$

If the vibrating molecules are irradiated with electromagnetic radiation with the electric field strength E and frequency ν_0, as defined by Equation 4, an electric dipole moment P can be defined by Equation 5, where α is the polarizability.

Equation 4: $E = E_0 \cos(2\pi \nu_0 t)$

Equation 5: $P = \alpha E_0 \cos(2\pi \nu_0 t)$

The polarizability is a linear function of the displacement at small amplitudes. Therefore one can approximate the polarizability about the equilibrium position using a 1st order Taylor series approximation as seen in Equation 6, below, where $\left(\frac{\partial \alpha}{\partial q}\right)_0$ is the change in polarizability with respect to displacement at the equilibrium position..

Equation 6: $\alpha = \alpha_0 + \left(\frac{\partial \alpha}{\partial q}\right)_0 q_0$

One can then combine equations Equation 1 to Equation 6 in order to solve for the dipole moment P, as seen in Equation 7 below.

Equation 7:

$$P = \alpha_0 E_0 \cos(2\pi \nu_0 t) + \frac{1}{2}\left(\frac{\partial \alpha}{\partial q}\right)_0 q_0 E_0 [cos\{2\pi(\nu_0 + \nu_m)t\} + cos\{2\pi(\nu_0 - \nu_m)t\}]$$

From Equation 7, the term $\alpha_0 E_0 \cos(2\pi \nu_0 t)$ only relies on the frequency of the irradiating electromagnetic field. This term is responsible for the Rayleigh scattering. One can also see that the $2\pi(\nu_0 + \nu_m)t$ and $cos\{2\pi(\nu_0 - \nu_m)t\}$ terms rely on the difference between the frequency of the irradiating electromagnetic field and the natural frequency of the molecule. This is responsible for the anti-Stokes and Stokes Raman scattering, respectively. In anti-Stokes scattering, the irradiating electromagnetic field gains energy and decreases in wavelength. While in Stokes scattering, the irradiating

electromagnetic field loses energy and increases in wavelength. These phenomena can be seen in Figure 6 below.

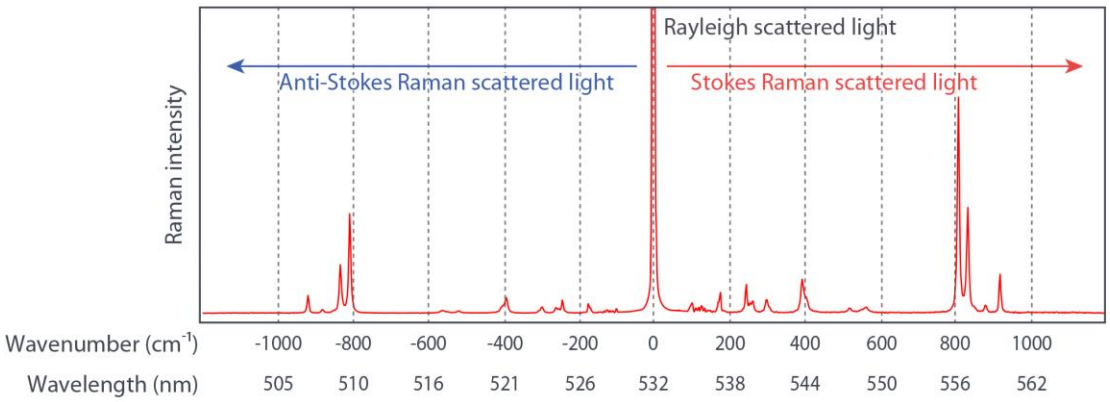

Figure 6: Raman spectra of ethanol [10].

Furthermore, one can also observe from the $\frac{\partial \alpha}{\partial q}$ term in Equation 7, that the Raman scattered light is dependent on the change in polarizability with respect to displacement. More specifically, a molecule is Raman active if the polarizability changes as a result of the natural vibrations of the molecule.

In molecules, the polarizability is a tensor and not a scalar. The changes in the polarizability tensor causes the Raman scattering. For simple molecules, one can visualize the polarizability tensor as an 3 dimensional ellipsoid by plotting $\frac{1}{\sqrt{\alpha_i}}$, as seen in Figure 7 below, where α_i represents the rows of the polarizability tensor. When the polarizability tensor is visualized as an ellipsoid, one can visually determine if a molecular vibration is Raman active by looking for asymmetric changes in the size, shape, or orientation of the ellipsoid under its vibrational modes [8].

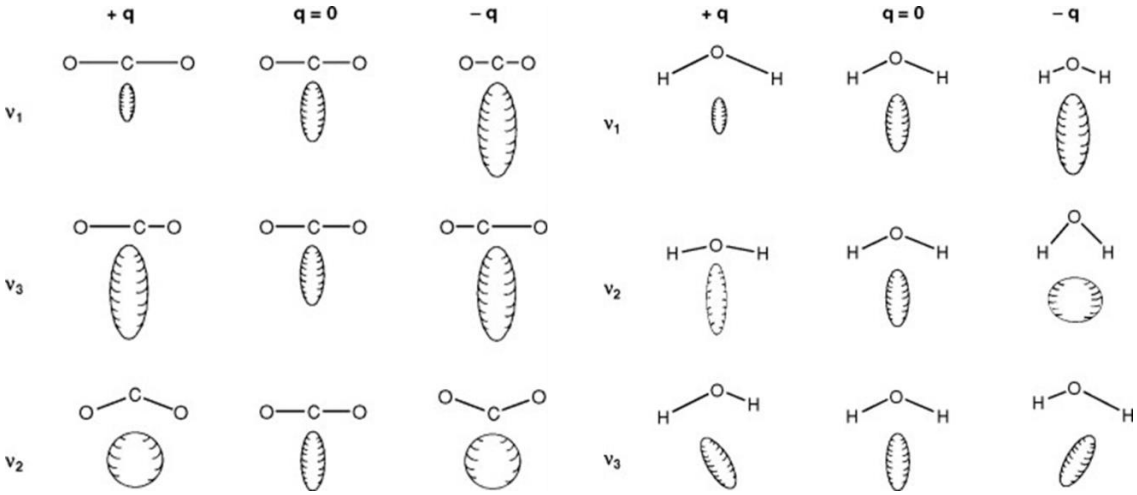

Figure 7: Polarizability ellipsoids for carbon dioxide (left) and water (right) [8].

From Figure 7, one can see that only vibrational mode v_1 is Raman active for carbon dioxide and that all vibrational modes of water are Raman active because the size, shape or orientation of the polarizability ellipsoid changes for all vibrational modes. In addition, vibrational mode v_1 of carbon dioxide is Raman active but not IR active because the vibration is symmetric relative to its center of symmetry. Along an axis of symmetry, a mode cannot be both IR and Raman active. This is referred to as the rule of mutual exclusion. The Raman scattering and IR fluorescence activity of complex molecules can be predicted using point group analysis and characteristic tables [8].

One can describe the physics of Raman scattering through the use of a Jablonski diagram that shows the electronic state of the molecule. This can be seen in Figure 8, below. In this figure, one can see that in Rayleigh scattering, the molecule interacts with the irradiating light, is excited into a virtual state between the two energy levels, and then relaxes back to its original state. In Stokes Raman scattering, one can see a similar process except that the molecule returns to an exited state. The energy difference is due to the Raman scattered light losing energy to the molecule and increasing in wavelength in

an inelastic process. In anti-Stokes Raman scattering, the molecule returns to a lower energy state due to the Raman scattered light gaining energy from the molecule and decreasing in wavelength. Resonance Raman is a similar process as the normal Raman process except the molecule is excited to a state that is in the next energy level. This is due to the irradiating light having an energy that is close to that of the electronic transition [8].

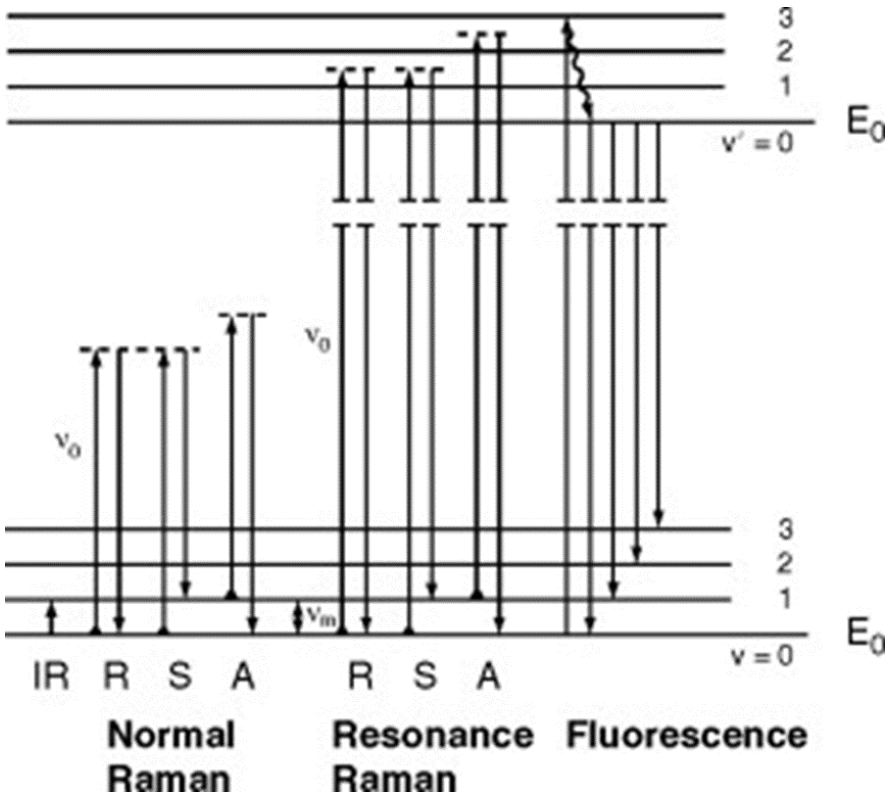

Figure 8: Jablonski diagram showing the process of Raman scattering [8].

2. Thermometry Through Far-Field Raman Spectroscopy

2.1. Application of Raman Thermometry to HAMR studies

2.1.1. Introduction

We propose that Raman thermometry be used to both replicate the laser heating in HAMR drives and measure peak temperature of HAMR recording media. The excitation laser of the Raman spectrometer can be used to replicate HAMR-like laser radiation. In a similar fashion to an actual HAMR drive, the laser radiation will heat a recording media sample. The resulting Raman scattering from the media sample can then be analyzed for thermal properties and changes in chemical composition.

Raman spectroscopy allows one to measure the temperature of an object without having to contact the object with a physical probe. In addition to the noncontact nature of thermometry though Raman spectroscopy, the excitation laser used in the temperature measurement can cause heating of the sample when the excitation laser has significantly high electromagnetic flux. This thermal aspect of Raman thermometry is considered a drawback in many cases, but the laser heating can be exploited as a key advantage when applied as a method for studying materials used in heat-assisted magnetic recording (HAMR).

While it is known that the thermal and electromagnetic conditions generated by current Raman spectroscopy techniques may not be completely identical to those found in the head-disk interface of a HAMR drive, it is expected that data gathered from the

combined electromagnetic heating and Raman spectroscopy technique could be used in a model that can accurately predict the degradation of materials used in HAMR drives. The collected data can be combined with numerical modeling, previous component and drive level testing, and additional analytical techniques to create a model that can be used to prequalify materials and thin film structures before more complex and extensive testing occurs.

The proposed method of thermometry and simulation of HAMR-like radiation has the benefits of being a rapid, cost-effective, and highly controlled way of analyzing a material's resistance to damage from exposure to HAMR-like laser radiation. By accurately modeling and predicting material and structural resistance to HAMR radiation damage, one can more easily design and select materials and thin film structures for use in HAMR drives. One can circumvent the need to construct a large number of working HAMR heads and associated components to initially test the viability of a material for use in HAMR drives. Thus, by using Raman spectroscopy to both simulate and measure the conditions occurring in a HAMR drive, one can reduce the time and expense required per design iteration and increase the speed at which one can introduce new HAMR technologies to the market.

2.1.2. Methods for Measuring Temperature using Raman Spectroscopy

There exist multiple Raman spectroscopy techniques that can be used to determine the temperature of on object. Common techniques include measuring the intensity ratios of the Stokes and anti-Stokes Raman scattering, changes in the full width at half maximum (FHWM) of the peaks of the Raman spectra as a function of

temperature, and changes in the peak positions of the Raman spectra as a function of temperature [11]. Of these methods, measuring the intensity ratios of the Stokes to anti-Stokes Raman scattering is the most straightforward method as the intensity ratio is well defined by the Boltzmann distribution for materials that do not experience the hot-phonon effect [11], where the phonons exhibit a nonequilibrium distribution [12]. This method only requires a typical calibration of the spectrometer such as those outlined in *ASTM E2911-13* [13]. A drawback of the method using Stokes to anti-Stokes scattering ratio is that spectrometers with the proper optical filters for measuring both the Stokes and anti-Stokes Raman scattering are less common than spectrometers that can only measure the Stokes Raman scattering. For the studies in this thesis, a Raman spectrometer that could only measure Stokes Raman scattering was used.

With the spectrometer limitations in mind, we chose the thermometry method using changes in the peak positions of the Raman spectra. This was the optimal way to measure temperature with only the Stokes Raman scattering because the spectrometers that were available had the necessary spectral resolution to measure small changes in the peak positions in the Raman spectra. In addition, the peak positions in terms of wavenumber shift can be easily found through spectral deconvolution techniques such as Voigt profile deconvolution, where functions, represented by a convolution of Gaussian and Lorentzian functions, are numerically fitted to the spectra [14].

Although there already exists examples of research using the peak shift in the Stokes Raman spectra to measure the temperature of carbon films [15], the relationship between the peak position and sample temperature has to be established specifically for the hard disk sourced diamond-like carbon (DLC) material used in the experiments in this

thesis. As mentioned in the previous chapters, Raman scattering is a vibrational phenomenon that is related to the molecular and electronic structure of the substance exhibiting the scattering. Therefore, differences in crystal structure, bond hybridization, and inclusion of other substances such as nitrogen and hydrogen can greatly affect the Raman spectra of the carbon [16]. With this knowledge, one can conclude that, in order to generate an accurate temperature versus Stokes Raman peak shift, one must generate a material specific correlation between the known sample temperatures and the resulting Stokes Raman peak shifts. The resulting correlation between sample temperature and resulting Raman shift can be used as a calibration curve to measure the unknown temperature of a sample.

2.2. Calibration of Raman Shift Thermometry Technique

2.2.1. Principles of the Measurement Technique

The characteristics of the Raman spectra of a sample can be affected by numerous factors. Most notably, temperature and stress can affect the vibration properties of the bonds and crystal lattices in a material and therefore can influence the Raman scattering of the material. Beechem et al. have noted the coupled effects of temperature and thermal stress on Raman spectra and have successfully developed a measurement technique that can account for both effects, thereby allowing simultaneous temperature and stress measurements using the peak position and peak linewidth of Stokes Raman scattering. Beechem found that although the Stokes shifted peak positions of Raman spectra are

stress dependent, the full width at half maximum of the Raman peaks tends to be insensitive to stress [17].

While it may be possible to apply a method relying on FHWM linewidth similar to that described by Beechem et al., it was determined that using the Stokes shifted peak positions with a sample specific calibration curve was more appropriate. The samples of interest are diamond-like carbon (DLC) coated multi-layered thin film structures, similar to the media that would be used in heat-assisted magnetic recording drives. By the nature of how thin the DLC film is, the Raman spectra tend to exhibit low signal to noise ratio due to the shear lack of DLC material. Furthermore, the low signal to noise ratio makes it more difficult to accurately measure the linewidth versus measuring the peak position. This factor makes it difficult to apply the measurement linewidth technique described by Beechem, et al. Therefore, it was decided that corelating temperature to a sample specific peak position calibration curve, similar to the results published by both Beechem [17] and Cui et al. [15], would be the most optimal approach to determining temperatures in the sample of interest.

In order to generate the calibration curve, an experimental setup similar to the one used by Cui, et al. [15] was constructed. This experimental setup is based on far-field Raman spectroscopy and does not generate the desired HAMR-like radiation conditions mentioned in the previous sections. Rather, the experimental setup was used to test the feasibility of using methods similar to the ones used by Cui, et al. [15] on amorphous carbon materials similar to those used in hard disk drives.

2.2.2. Experimental Setup

The experimental setup consists of a heated microscope stage that is placed inside a Renishaw RM1000 confocal micro-Raman spectrometer. Inside the heated stage, a sample holder secures a diamond-like carbon (DLC) coated sample of interest. The DLC sample is heated to known temperatures by the stage and the calibration is conducted in accordance to the procedure outlined in the previous chapter.

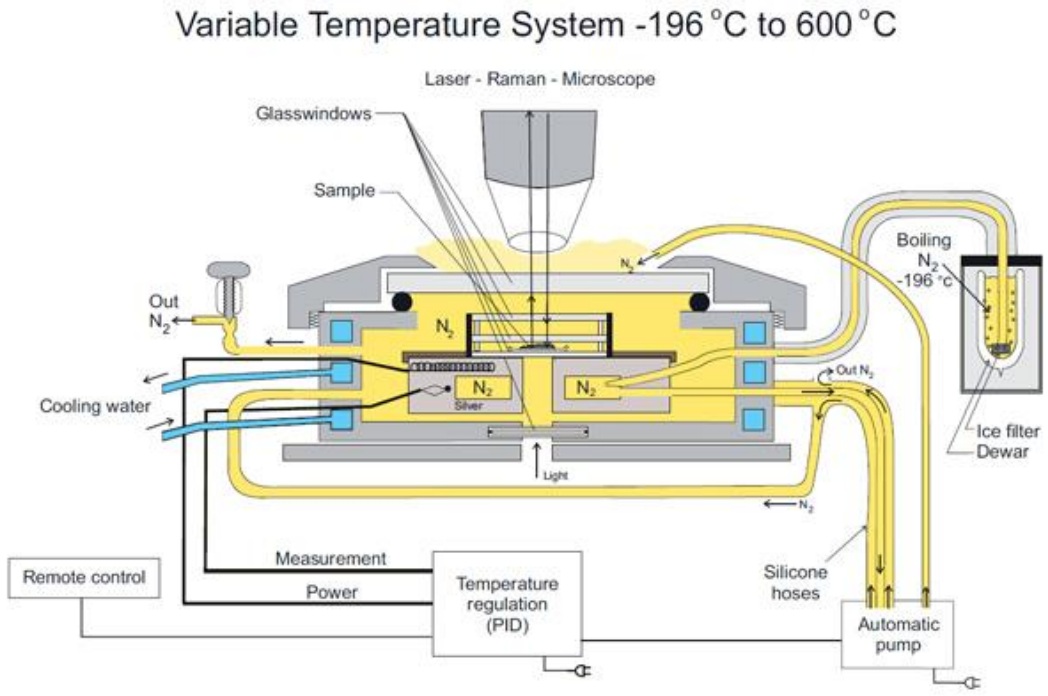

Figure 9: Example of a Linkam brand thermal stage for Raman spectroscopy [18].

Commercial manufacturers, such as Linkam Scientific Instruments Limited, produce heated stages that are capable of being used in the calibration procedure mentioned in the precious sections. An example can be seen in Figure 9 above. In general, these stages operate by heating the sample to a high temperature and then using a

combination of water and boiled liquid nitrogen to protect surrounding equipment from thermal damage. Commercially available stages have the disadvantages of being costly, requiring liquid nitrogen, and requiring circulating chilled water. These disadvantages along with their high cost prevented the implementation of a commercial stage in our experimental setup.

Instead of purchasing a commercial stage, a custom stage was made for the Raman spectrometer used in this experiment. The custom stage was required to be able to heat the samples to about 1000 degrees centigrade, accurately measure the temperature of the heated samples, and resist excessive thermal fluctuations from changes in the external environment. In addition, the custom stage had to fit under the Raman spectrometer's microscope, protect the Raman spectrometer from thermal damage, and allow the heated sample to be placed within the working distance of the microscope. These design factors were considered, and an initial design was created on Solidworks.

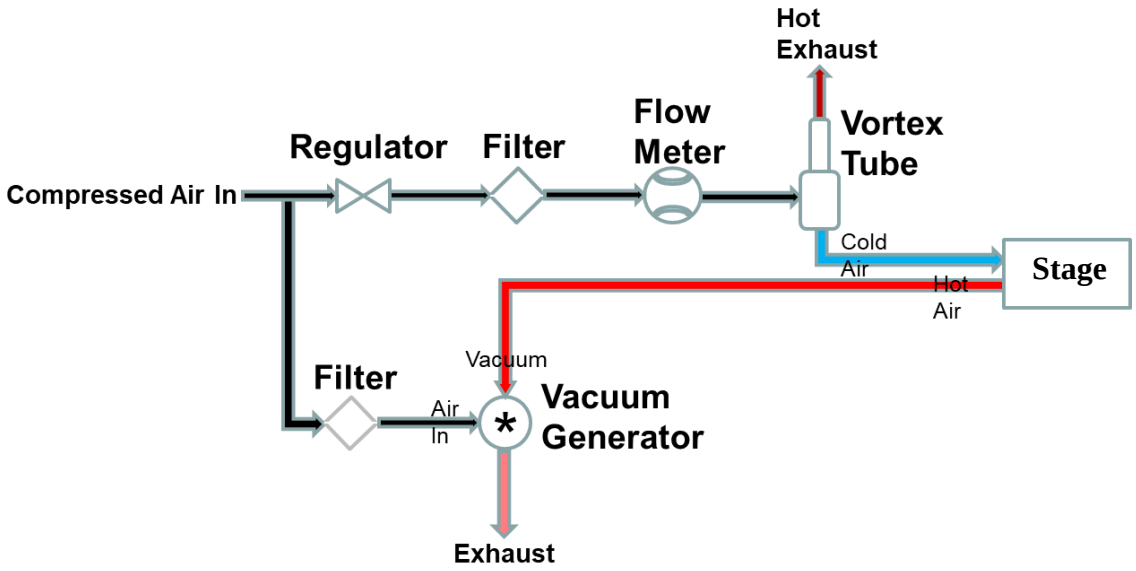

Figure 10: Cooling circuit diagram of the thermal control stage.

The initial design used compressed air to cool the heated microscope stage and protect the optics of the Raman spectrometer. Refrigerated compressed air enters the heated microscope stage from one port, flows over the sample holder, and is suctioned out from an opposing compressed air port. A portion of the compressed air is not evacuated by the vacuum. Instead, the air exits the top of the heated stage in order to cool the microscope objective to protect it from excessive heat. Vacuum was provided a high-volume venturi-style vacuum generator. Refrigerated compressed air was provided by a Ranque-Hilsch vortex tube. A schematic of the design can be seen in Figure 10 above.

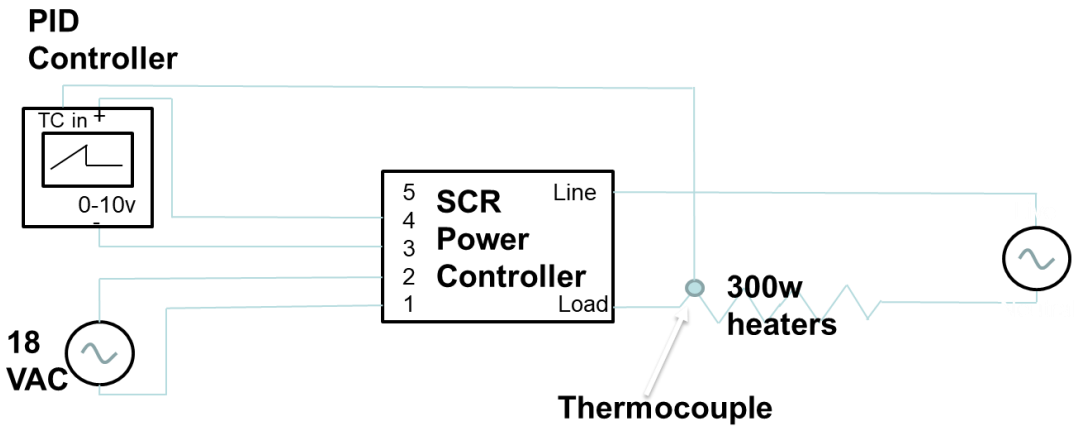

Figure 11: Circuit diagram of the heating and temperature regulation system of the thermal control stage.

In the initial design, heat is provided by two 150-watt Inconel AC cartridge heaters purchased from Omega Engineering. Both heaters are embedded in a copper heat spreader to reduce thermal gradients in the sample undergoing heating. The heat spreader has an indentation that physically secures the sample and acts as a sample holder. In addition to the heaters, an Inconel covered k-type thermocouple is placed in the heat

spreader directly under the sample holder. This is used to accurately measure the temperature of the sample. A schematic of the design can be seen in Figure 11 above.

To protect the aluminum body of the heated stage, the sample holder was enclosed in calcium silicate ceramic insulation. The insulation allows for reduced heat input in to the system and creates a sharp thermal gradient between the aluminum stage body and the heat spreader. This thermal gradient prevents the aluminum body from reaching its melting point while allowing the heat spreader to reach temperatures far above the melting point of aluminum. A fused silica window at the top of the insulation layers provided optical access to the heated sample. A CAD model of the design can be seen in Figure 12 below.

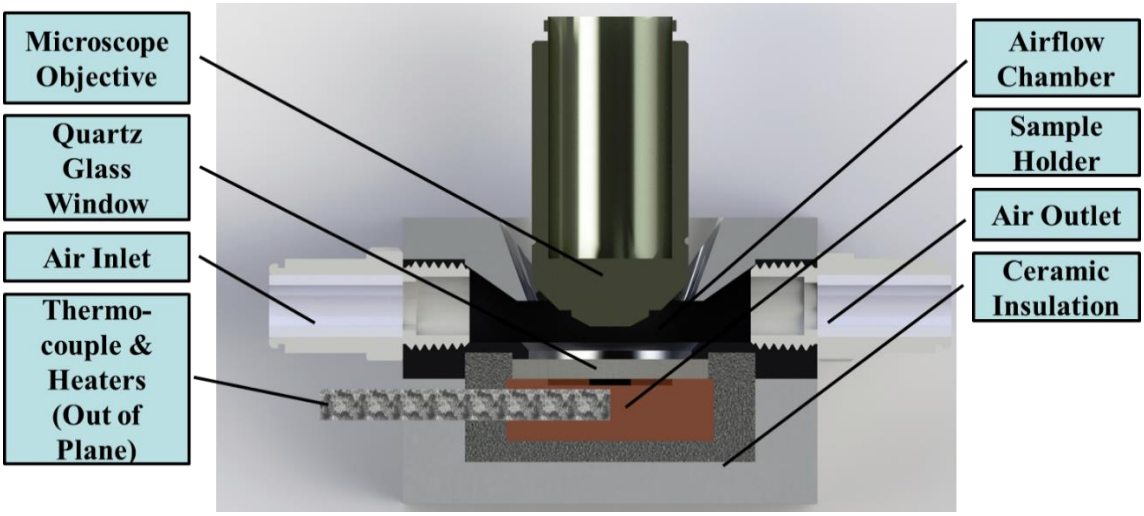

Figure 12: Cutaway of a CAD model of the initial thermal stage design.

Thermal simulation of the initial design can be seen in Figure 13 below. The airflow through the heated stage was incrementally increased to see how much flow is required to cool the stage to safe temperatures. The simulation showed that the desired

amount of cooling was not obtainable with realistic airflows. Therefore, a second design was created.

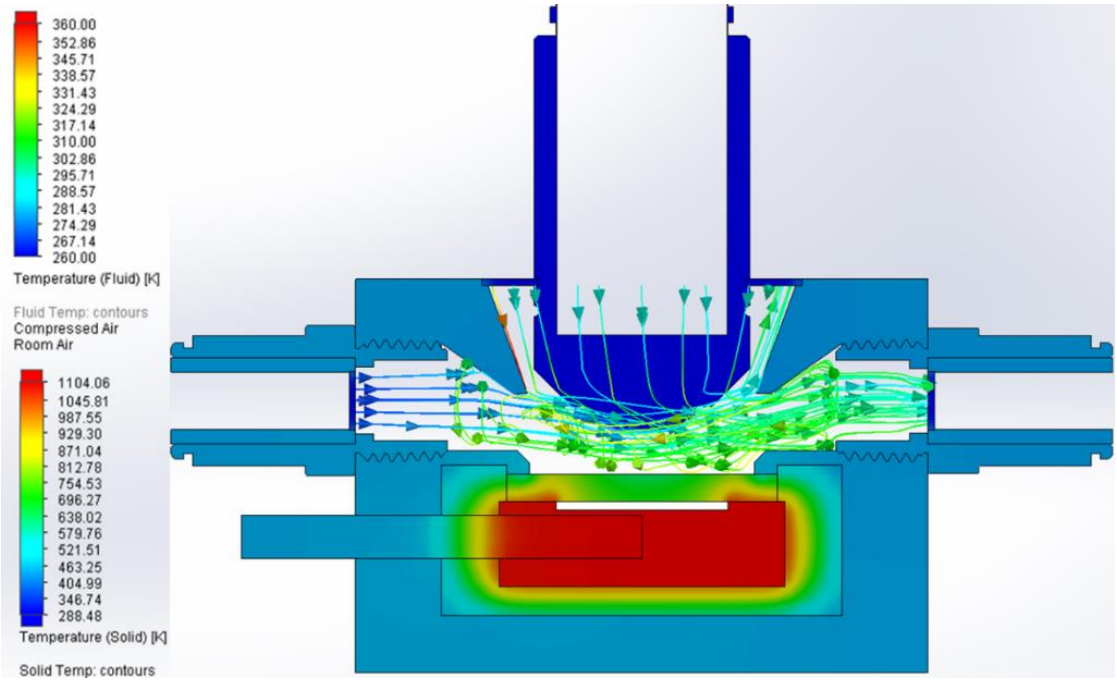

Figure 13: Thermal simulation of initial stage design.

The second design added a commercially available computer water cooling block. A computer-aided design (CAD) model of the second design and a conjugate heat transfer simulation of the proposed design can be seen in Figure 14 below. The second design functions by flowing ice water from an insulated container to a water-cooling block to remove large amounts of heat. Simulations showed that the addition of the water-cooling block is effective at reducing temperatures in the heated stage and Raman spectrometer to acceptable levels. The water-cooled design has the drawback of using a system that has the potential to leak water and of being a tall system that requires

additional mounting hardware to fit under the Raman spectrometer's microscope. These drawbacks justified the creation of a third and final design revision.

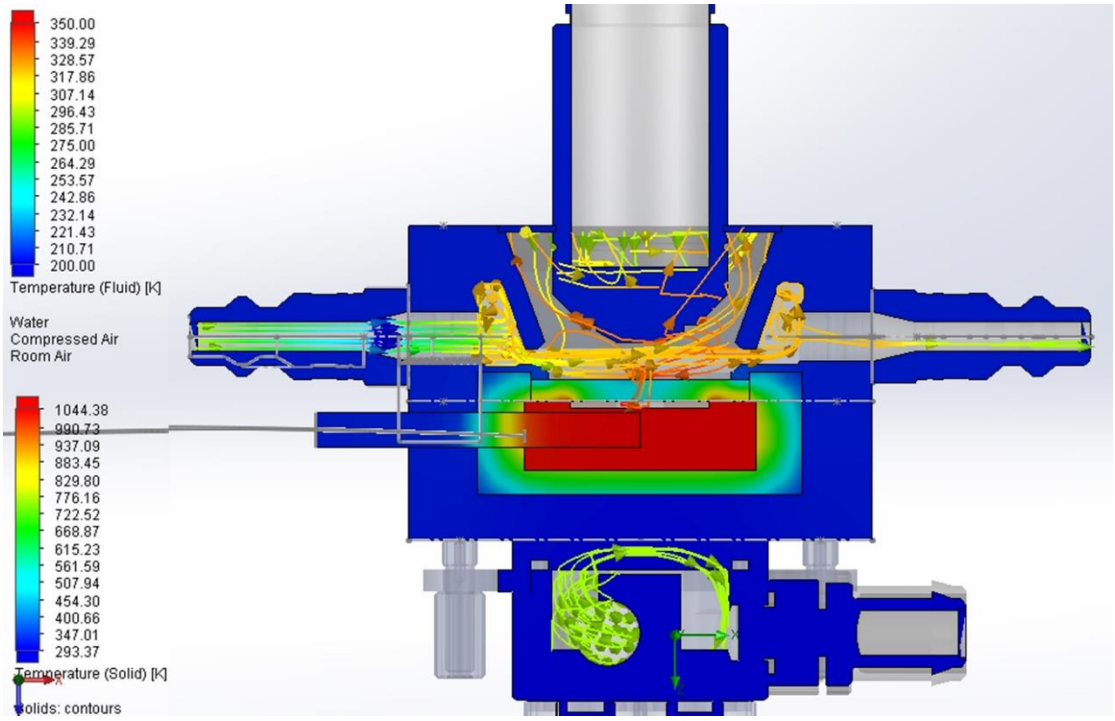

Figure 14: Thermal simulation of simulaneous air and water cooled thermal stage.

The third and final design was similar to the initial design except that additional flow channels were added, and the heat spreader was modified. A CAD model of the final design and a conjugate heat transfer simulation of the proposed design along with the manufactured system can be seen in Figure 15 and Figure 16 below. Air flow channels of the final design were enlarged to allow a larger volume of air to flow through the system. Additional flow channels were added below the ceramic insulation and pillars were added to the channel to increase the heat transfer area between the heated areas and the air flow. The material of the heat spreader was changed from copper to titanium. Copper is prone to oxidation at high temperatures. Additionally, copper has a relatively

high coefficient of thermal expansion and may cause cracking in the brittle ceramic insulation that surrounds the heat spreader. Invar 36 was initially chosen as a replacement material due to its extremely low coefficient of thermal expansion, but the material is not widely available and is not machinable with the tools available to the laboratory. Titanium offers a good balance of low coefficient of thermal expansion, oxidation resistance at high temperatures, availability for purchase, and machinability. Simulations showed that the final design provided adequate cooling. After construction of the heated stage, the simulations were then verified to be within tolerances by probing the stage with a thermocouple.

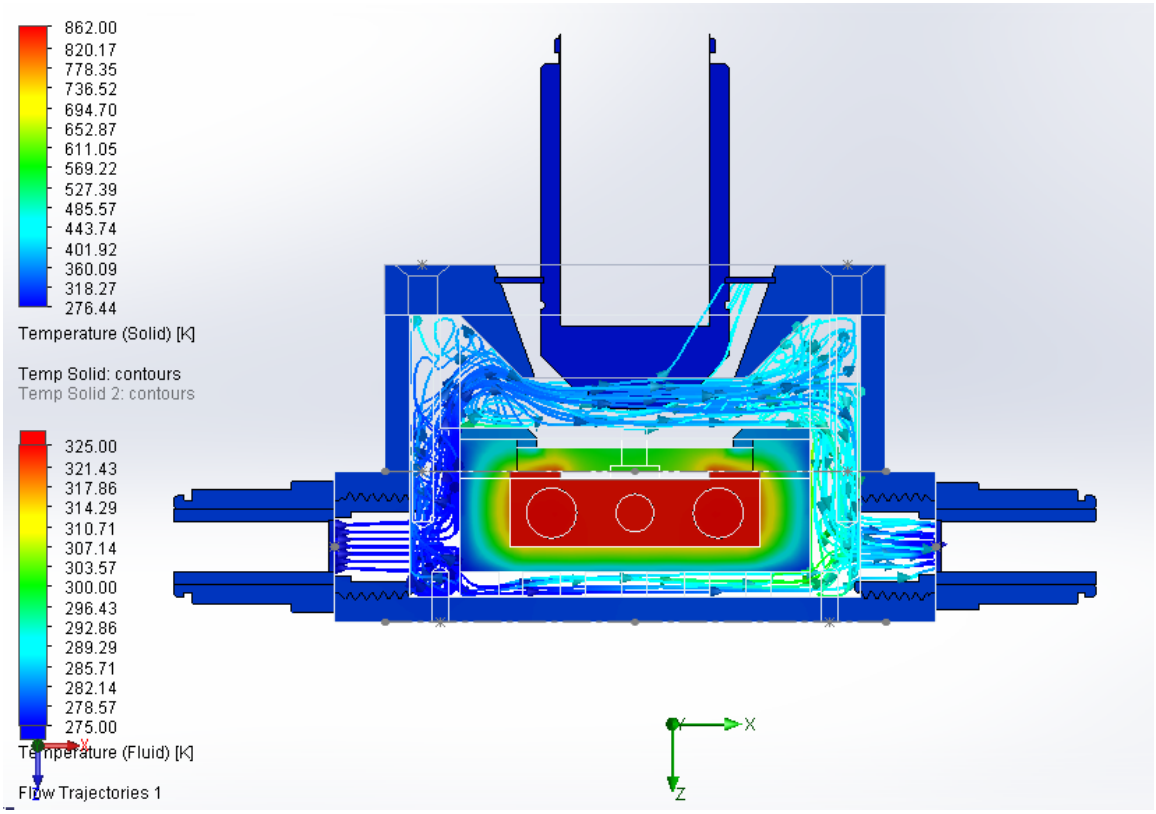

Figure 15: Thermal simulation of thermal control stage as manufactured.

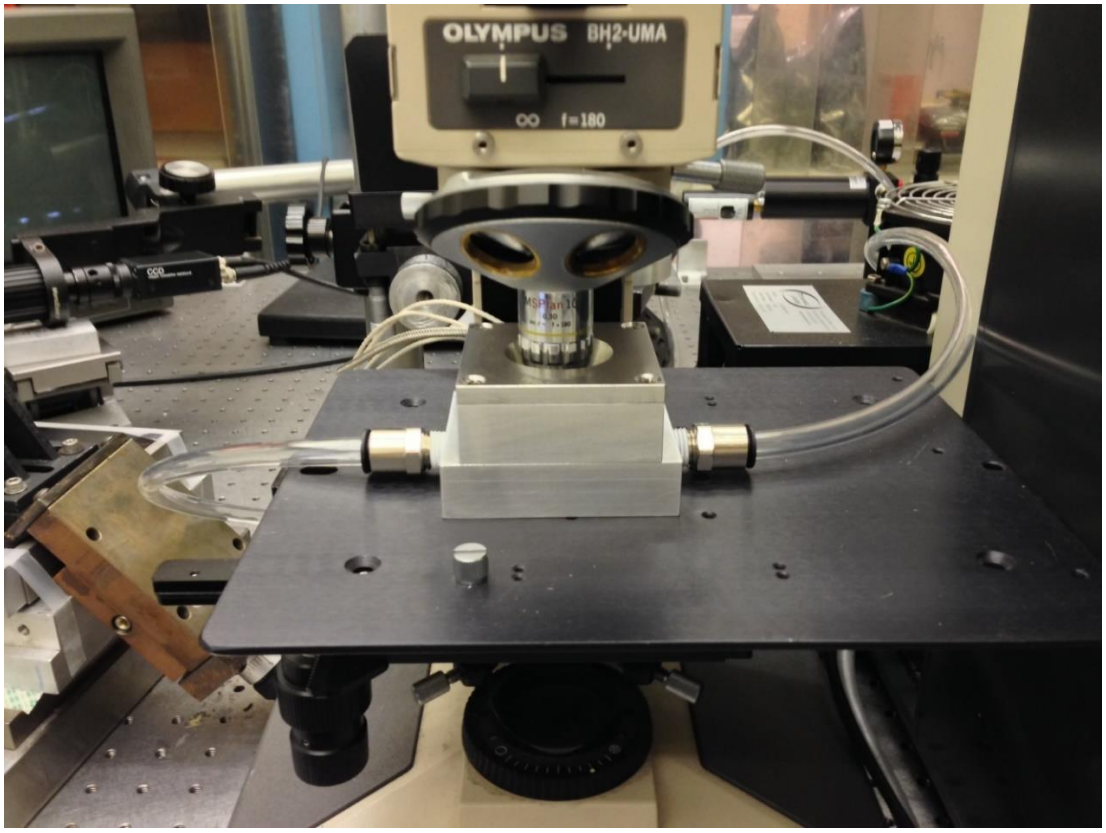

Figure 16: Photograph of thermal control stage.

2.2.3. Experimental Procedure

The experiment used diamond-like carbon (DLC) coated steel samples. The DLC was deposited using filtered cathodic vacuum arc deposition by another laboratory. Multiple samples were obtained with thickness of the DLC ranging from 20nm to 690nm. The substrate below the DLC was AISI 4140 steel. Samples of each thickness were thermally cycled in the heated stage at temperatures ranging from room temperature to 800 degrees centigrade. Each cycle involved heating the sample from room temperature to a target temperature and then allowing the sample to cool and return to room temperature. The cycle was repeated for a single sample until the maximum target

temperature was reached. A Raman spectrum was collected each time a target temperature was reached and at each time that the sample returned to room temperature. A diagram of the cycle can be seen in Figure 17 below.

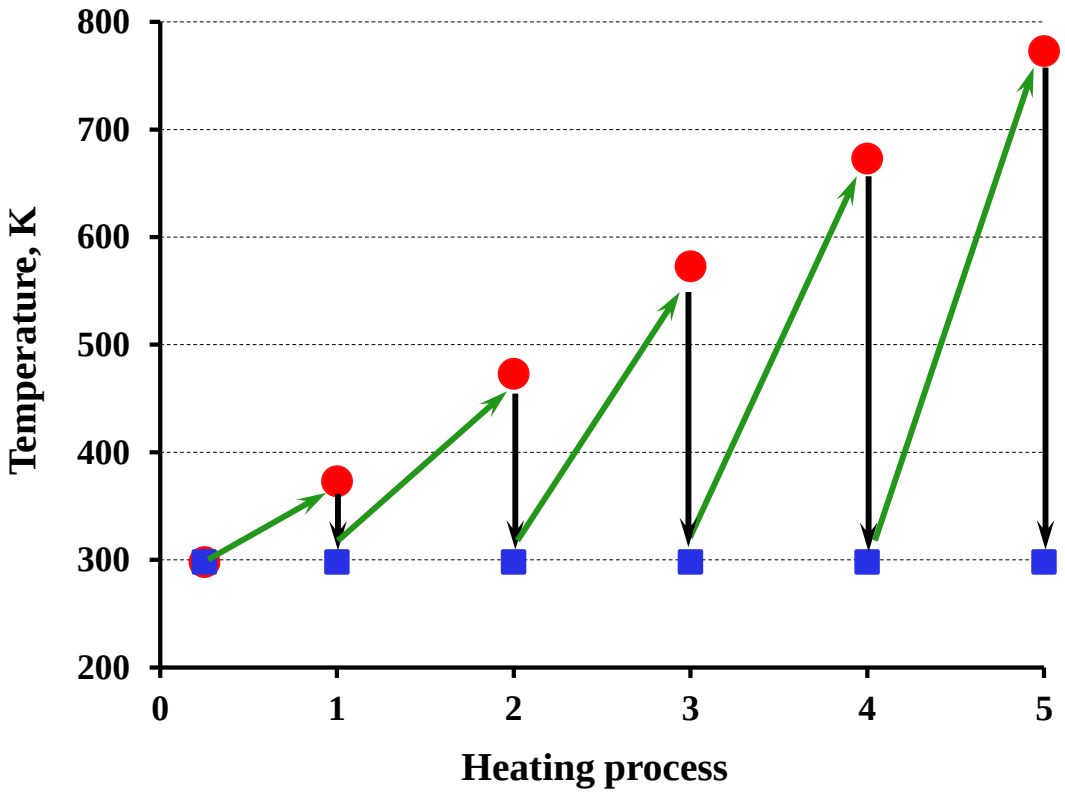

Figure 17: Diagram showing multiple thermal cycles from room temperature to target temperature and back. Previously published in [19].

2.2.4. Results

Conclusive results were obtained from the 690nm DLC sample. Thinner DLC samples produced inconclusive results due to their low signal to noise ratio. It is suspected that the thinner samples exhibited lower Raman cross sections due to the lack of material in the direction of the probing light.

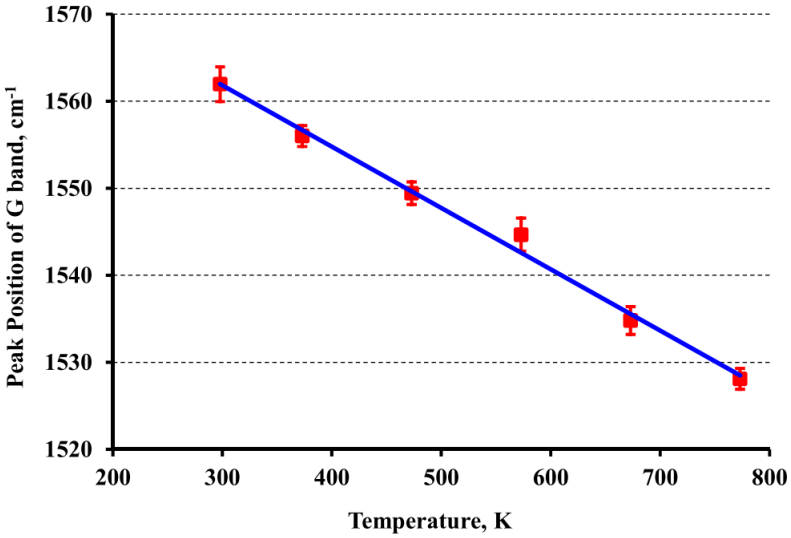

Figure 18: Plot of the Raman G peak position, caused by sp^2 carbon bonding, as a function of maximum exposed temperature, when measured during temperature exposure, for the 690nm thick DLC coated sample. Previously published in [19].

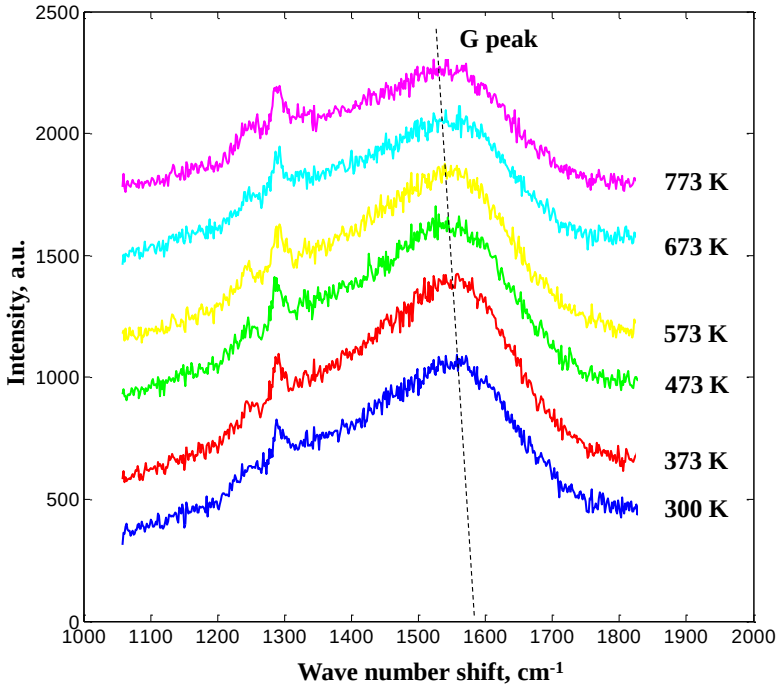

Figure 19: Raman spectra of the 690nm thick DLC sample showing a decrease in wavenumber shift as a function of maximum exposed temperature, when measured during temperature exposure. Previously published in [19].

The 690nm samples displayed a clear correlation between the G peak of the Stokes Raman spectra, resulting from sp^2 hybridized bonds, and the target temperature during thermal cycling.

As seen in Figure 18 and Figure 19 above, the G peak of the 690nm DLC's Raman Spectra exhibits a lower wavenumber shift as a function of maximal temperature during the thermal cycle, when measured during the exposure to the maximal temperature. In addition, as seen in Figure 20 and Figure 21, below, the G peak of the sample exhibits a higher wavenumber shift when measured at room temperature after the heating cycle has completed.

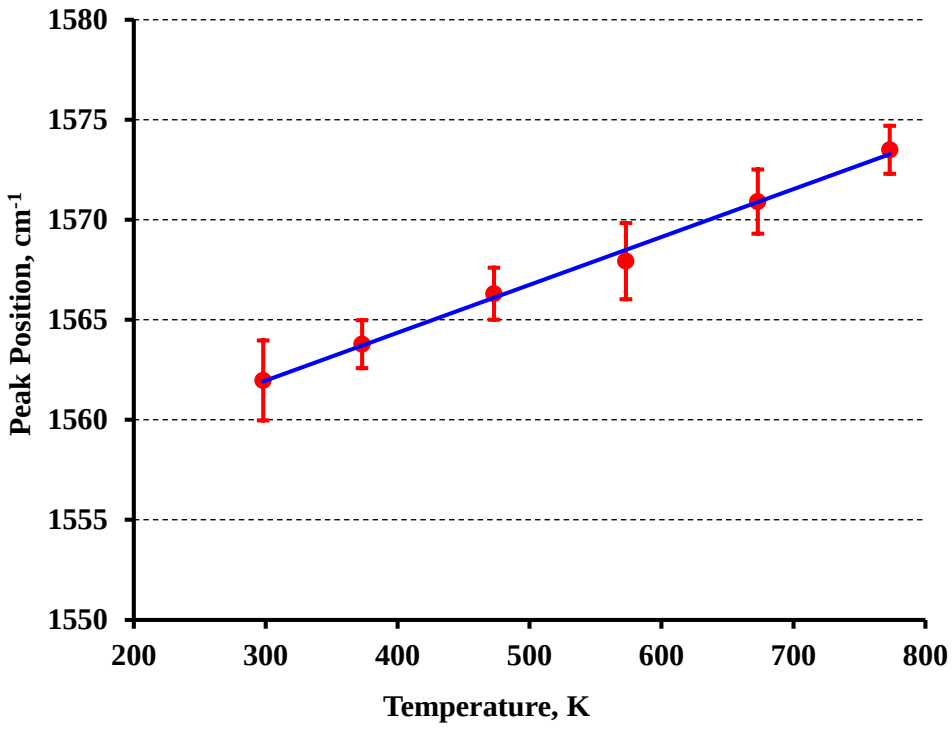

Figure 20: Plot of the Raman G peak position as a function of maximum exposed temperature, when measured after temperature exposure, for the 690nm thick DLC coated sample. Previously published in [19].

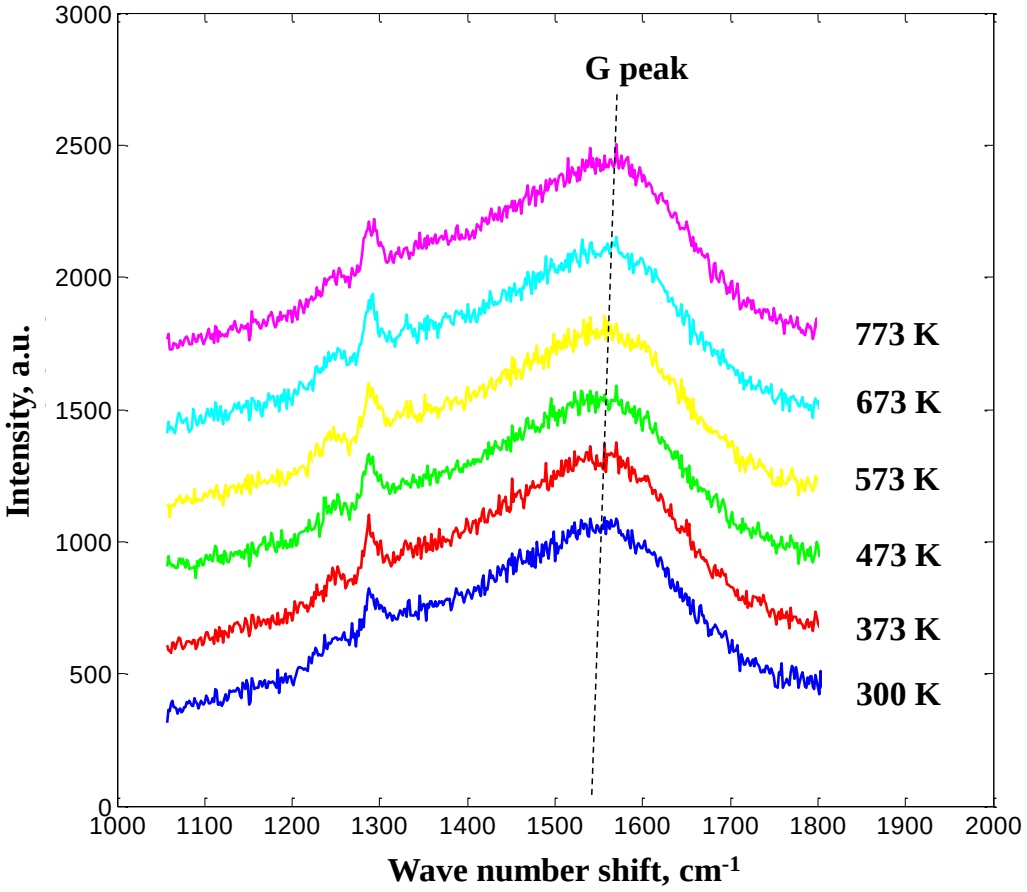

Figure 21: Raman spectra of the 690nm thick DLC sample showing an increase in wavenumber shift as a function of maximum exposed temperature, when measured after temperature exposure. Previously published in [19].

2.2.5. Conclusions

The results gathered from the calibration experiment roughly correspond to those published in the literature. Wang et al. studied the effects of rapid thermal cycling on samples with thin film DLC coatings, similar to those in hard disk drives, using Raman spectroscopy along with other analytical techniques [21]. Similar to the results found by our experiments, Wang's study had also found that, after thermal cycling, the G peak of the DLC's Raman spectra exhibited an increase in wavenumber shift as a function of the peak temperature that the sample was exposed to. Wang concluded that the changes in

the Raman spectra were a result of graphitization where sp^3 bonds transform into sp^2 bonds in addition to oxidation, changes in sp^2 cluster size, depletion of hydrogen, and changes in the ordering of the carbon network. We surmise that the results gathered in our own experiment result from the same phenomena observed by Wang.

Results obtained by the calibration experiment show that it is possible to use Raman spectroscopy to measure the temperature of a heated sample both during and after cyclic heating. Although this may provide some utility to the analysis of thermal damage in HAMR drives, its accuracy may be limited by the fact that the damage caused by the HAMR laser is caused by both near-field photo-radiation and thermal effects. Additionally, the laser excitation used in the aforementioned experiment does not generate an electromagnetic field that exhibits the same intensity as that found in a HAMR drive. Thus, further experimentation was conducted in order to heat a DLC coated sample of interest with intense near-filed electromagnetic radiation while simultaneously measuring the sample's thermal and chemical changes.

3. Surface Enhanced Raman Spectroscopy

3.1. Principles of Surface Enhanced Raman Spectroscopy

3.1.1. Introduction

A possible way to generate electromagnetic radiation of extreme intensity similar to that found in a heat assisted magnetic recording, is by using surface enhanced Raman spectroscopy (SERS). In surface enhancer Raman Spectroscopy, nanoparticles are used to generate intense radiation similar to that generated by the plasmonic nearfield transducer used in heat assisted magnetic recording drives. Although the electromagnetic radiation in SERS is not localized to the scales found in heat assisted magnetic recording systems, this was seen as a rational starting point as it is relatively simple to conduct SERS studies versus tip enhanced Raman spectroscopy (TERS) studies. Furthermore, SERS allows one to see the differences in the Raman spectra between plasmon enhanced and far field techniques and to observe any potential experimental challenges that may arise due to the use of intense nearfield excitation found in TERS.

3.1.2. Theory of Surface Enhanced Raman Spectroscopy

Surface enhanced Raman spectroscopy provides enhanced Raman scattering due to the enhancement in intensity of the excitation laser's electromagnetic radiation. The generation of intense electromagnetic radiation in SERS is due to the formation of surface plasmon-polaritons (SSP) and localized surface plasmon-polaritons (LSP). Both

SSPs and LSPs are quasi-particles that represent quanta of charge density oscillations in a plasma [22].

In SERS, SSPs are formed though the interaction between the photons from the excitation laser and a metal/dielectric interface. At a planar metal/dielectric interface, the photons couple with surface plasmon modes of the interface to form an electromagnetic wave known as SSPs. The SSPs can only propagate along the surface of the metal/dielectric interface in the nearfield. Thus, the electromagnetic energy from the excitation laser is confined to a small volume and increases in intensity as a result [22].

Similarly, LSPs are formed through the interaction between photons from the excitation laser and a rough metal surface or a metallic nanoparticle [20]. LSPs can occur at planar interfaces, but this is extremely rare. The sub-wavelength features of the nanostructures exhibit surface plasmon resonance modes that are dependent on material, surrounding medium, geometry, and electromagnetic environment. Under the correct conditions, the excitation laser will induce localized surface plasmon resonance modes on the surface of the nanostructure and form LSPs. The efficient coupling of the excitation laser to the LSPs, the confinement of the LSPs to the nanostructure, and the low energy loss in the system enhances the electromagnetic field around the particle. When two particles, structures, or surfaces that exhibit LSPs or SSPs modes are placed in close proximity to each other, they can electromagnetically interact and couple with each other. This coupling of plasmon modes enhances the electromagnetic field within the gap. This phenomenon is known as a gap mode [22].

Since the intensity of the Raman scattered light scales by the power of 4 relative to the electromagnetic field used for excitation, the enhancement of the electromagnetic

field used for excitation by LSPs or SSPs has the potential to greatly increase the Raman cross section of a material [20].

3.2. Measurement of DLC samples using SERS

3.2.1. Experimental Approach

The goal of the SERS experiment was to both maximize the electromagnetic intensity of the excitation laser at the surface of a sample of DLC coated hard disk media and to increase the signal to noise ratio of the Raman scattered light from the interface. This was done so that one could gain insight into the behavior of DLC and its associated Raman scattering under electromagnetically enhanced illumination. In order to meet these goals, an optimal combination of laser excitation wavelength and SERS media must be selected.

The first procedure in conducting surface enhanced Raman spectroscopy was to select the excitation laser used in the technique. A search through the literature showed that diamond-like carbon (DLC) has a more distinct G-peak, in terms of FWHM, when excited with a shorter wavelength laser [23]. In addition, from initial experimentation on a multi-wavelength Raman spectroscopy system, it became clear that shorter wavelengths produced better signal to noise ratios. Thus, a 458nm argon-ion laser, the shortest wavelength laser available to the author, was chosen for the SERS experiments.

Once the excitation laser was selected, SERS nanoparticles and SERS substrates were chosen based on the wavelength of the excitation laser. 75nm silver nanospheres from nanoComposix Inc. were chosen due to their resonance wavelength of 459nm. Hard

disk drive media, silver coated silicon, and silver coated black silicon based on that seen in “Black silicon SERS substrate: Effect of surface morphology on SERS detection and application of single algal cell analysis” by Deng and Juang [24] was chosen. The silver coated silicon and black silicon substrates were selected as secondary samples to the hard disk drive media in case the hard disk drive media did not produce enough enhancement.

3.2.2. Experimental Methods

The first step in the experiment is to produce the silicon substrates onto which the silver nanoparticles would be deposited. Bare silicon wafers were used for the control sample and for creating s smooth planar silver surface. 100mm p-type <100> silicon wafers were used as the base silicon substrates. All silicon wafers were precleaned in sulfuric acid-based piranha in order to remove organic contaminants and in hydrofluoric acid in order to remove the native oxide layer before any additional processing. Black silicon was formed through an cryogenic inductively coupled plasma reactive ion etching (ICP-RIE) process. The process parameters for the ICP-RIE process are as follows: -110°C stage temperature, 30.5SCCM SF_6 flow, 27.5SCCM O_2 flow, 1000W ICP forward power, 4W RF forward power, 10mTorr chamber pressure, and 7 minutes etch time. The tool used for ICP-RIE was an Oxford Plasmalab 100. After processing the wafers, silver was deposited on the wafers. The silver was sputtered onto the wafers using a Denton Discovery 18.

Subsequently, diamond like carbon (DLC) was deposited on the substrate using plasma enhanced chemical vapor deposition (PECVD). The deposition of the DLC was conducted in an Oxford Plasmalab 80, configured for PECVD, using methane as a

gaseous precursor. The process parameters are as follows: 100mTorr chamber pressure, 20°C stage temperature, 50SCCM methane flow, 250W RF power, 60min total process time. This deposited 20nm of DLC as measured through ellipsometry.

Commercial 3.5 inch hard disk media manufactured by Showa Denko was then obtained. The exact details of the DLC on the hard disk media are proprietary. What is known is that the DLC is approximately 2-3nm thick, contains approximately 40% sp^3 carbon, and was deposited using a type of chemical vapor deposition or physical vapor deposition method.

Following the deposition of the DLC and the acquisition of hard disk drive media, 75nm silver nanoparticles were deposited on the samples using a Langmuir-Blodgett film technique. Before the deposition of the silver nanoparticles, the nanoparticles were washed of excess polyvinylpyrrolidone (PVP) through multiple rounds of centrifugation and redispersion in ethanol. After washing in ethanol, the silver nanoparticles were dispersed in chloroform. The suspension of silver nanoparticles and chloroform was then drop casted onto the surface of a water bath until it formed a uniform Langmuir-Blodgett film. A DLC coated sample was then immersed through the Langmuir-Blodgett film, into the water, and then pulled from the bath. A vacuum desiccator was then used to dry the sample. This process resulted in a monolayer-like coating of silver nanoparticles over the DLC coated samples. An illustration of the process can be seen in Figure 22 below.

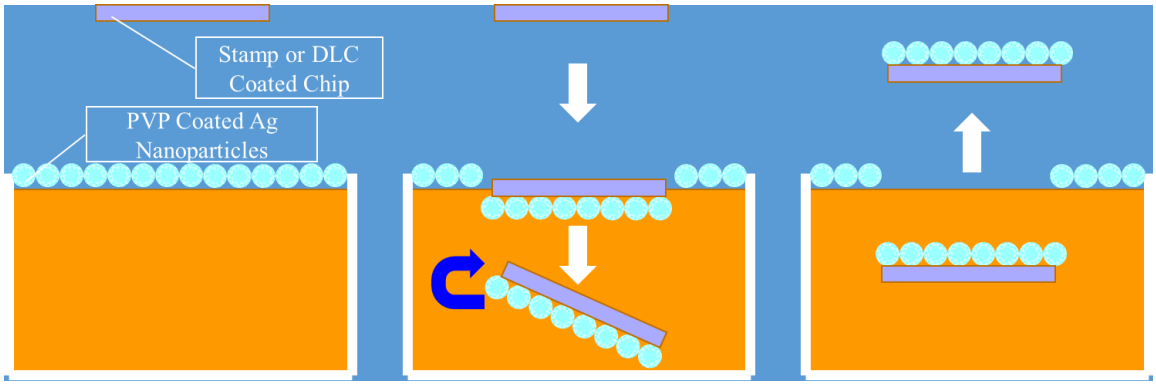

Figure 22: Illustration of the Langmuir-Blodgett film based nanoparticle deposition technique.

For the experiment, 10 samples were created, including the commercially available hard disk drive samples. The presence of a silver coating under the DLC, the presence of black silicon, and the presence of silver nanoparticles above the DLC was varied from sample to sample. An illustration of the sample variants can be seen in Figure 23 below.

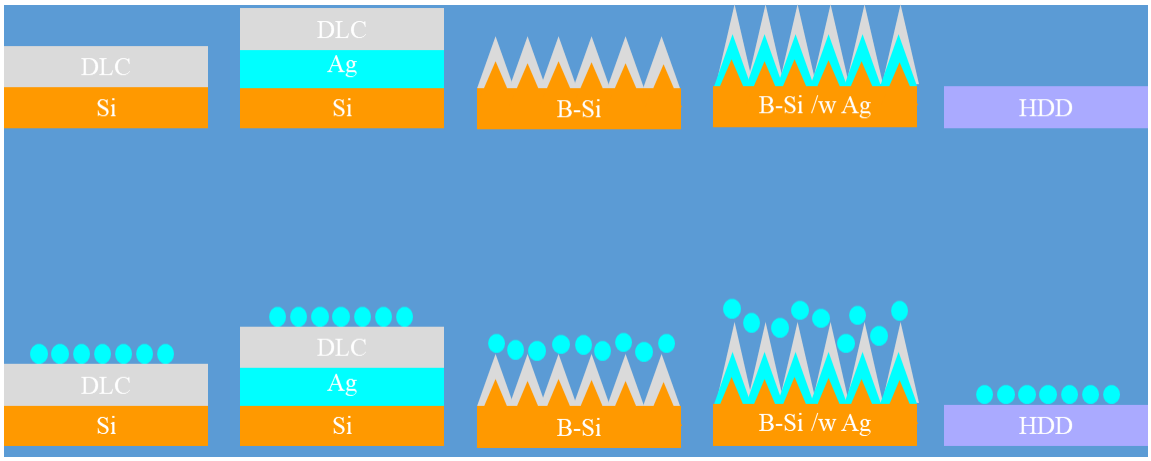

Figure 23: Illustration of sample variants

3.2.3. Results

Scanning electron microscopy analysis showed that the silver nanoparticles from the Langmuir-Blodgett film based deposition method produced regions on the sample that varied in silver nanoparticle concentration. This can be seen in Figure 24, Figure 25, and Figure 26 below.

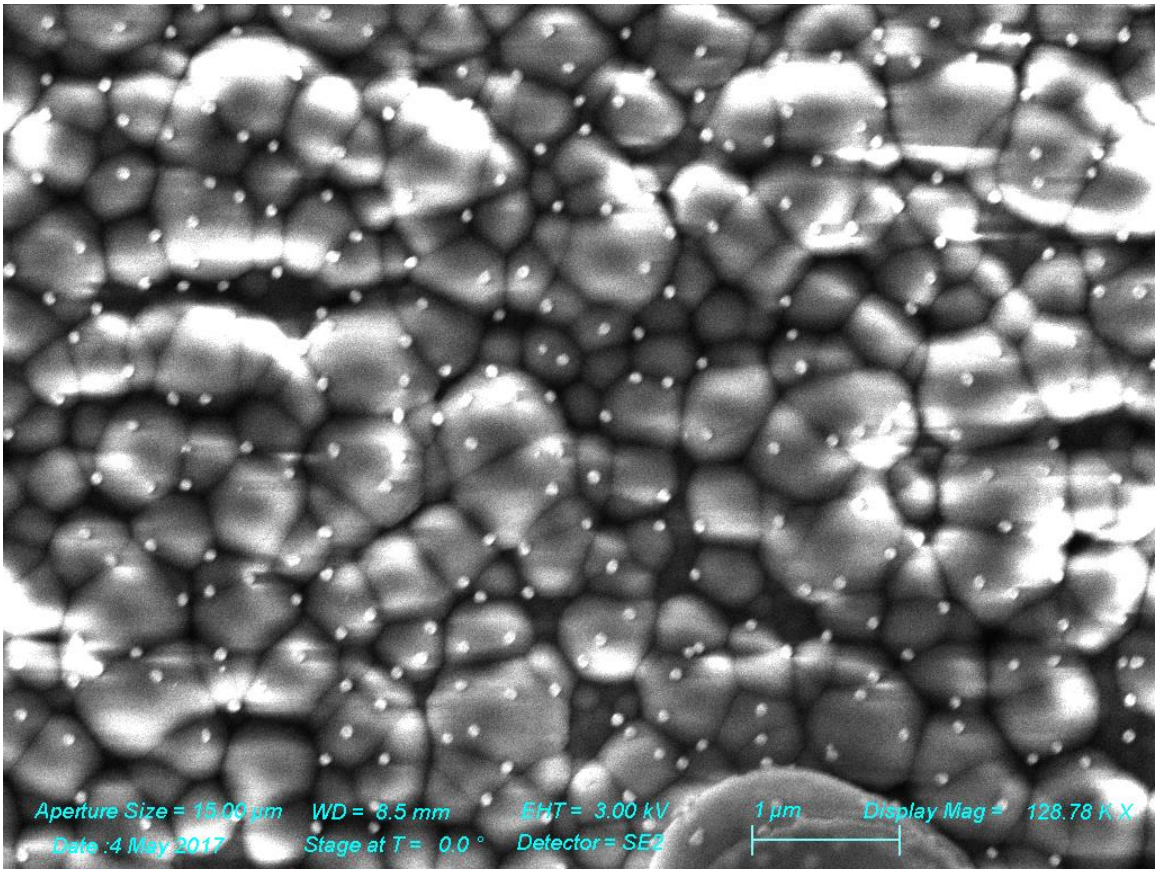

Figure 24: DLC coated sample with silver substrate and low density silver nanoparticle coating.

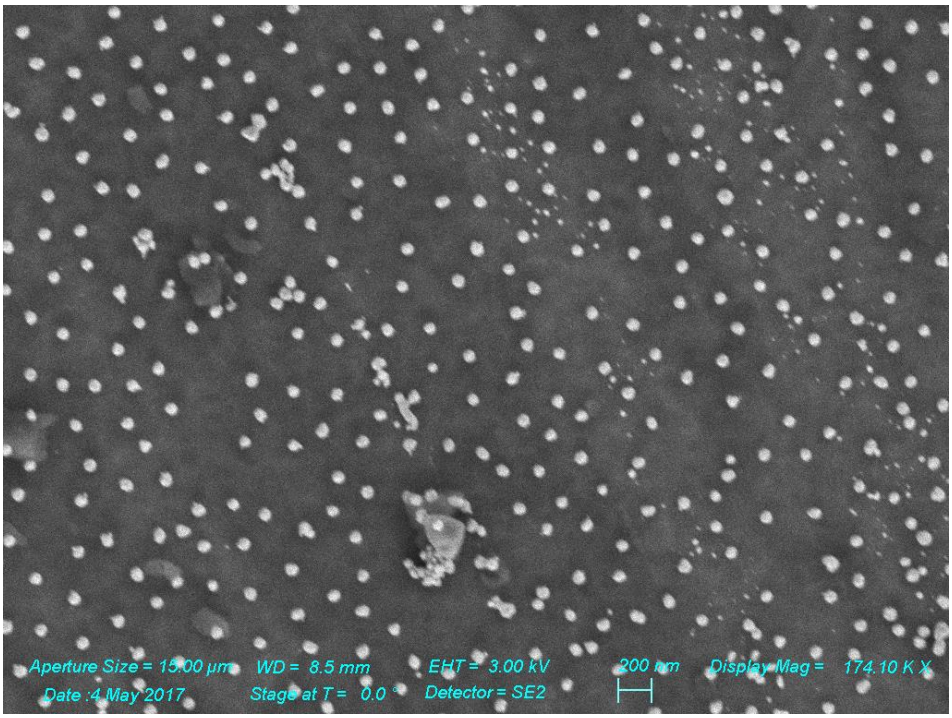

Figure 25: DLC coated sample with bare silicon substrate and moderate density silver nanoparticle coating.

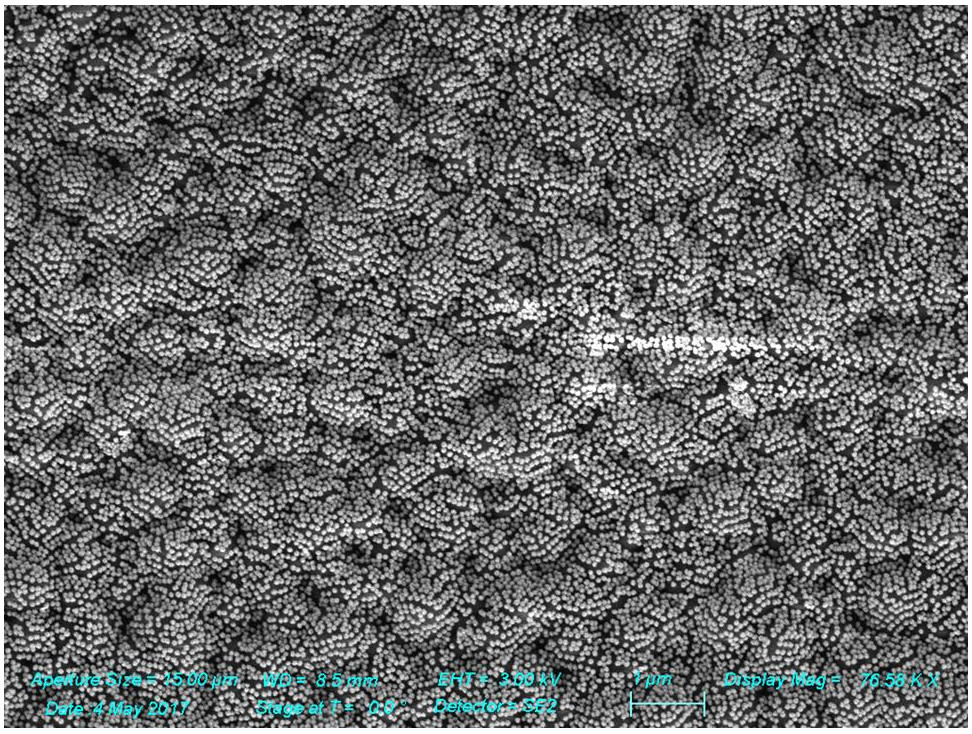

Figure 26: DLC coated sample with silver substrate and high density silver nanoparticle coating.

Through initial experimentation, it was found that the areas with high density silver nanoparticle coatings generated the greatest amount of enhancement of the Raman scattered light. Thus, the high-density areas were chosen for comparison of Raman signal enhancement.

The sample with the silver on silicon substrate and the commercial hard disk media showed strong signal enhancement of the D and G peaks of the Raman spectra. The spectra can be seen in comparison with their non-nanoparticle-coated controls in Figure 27 and Figure 28 below.

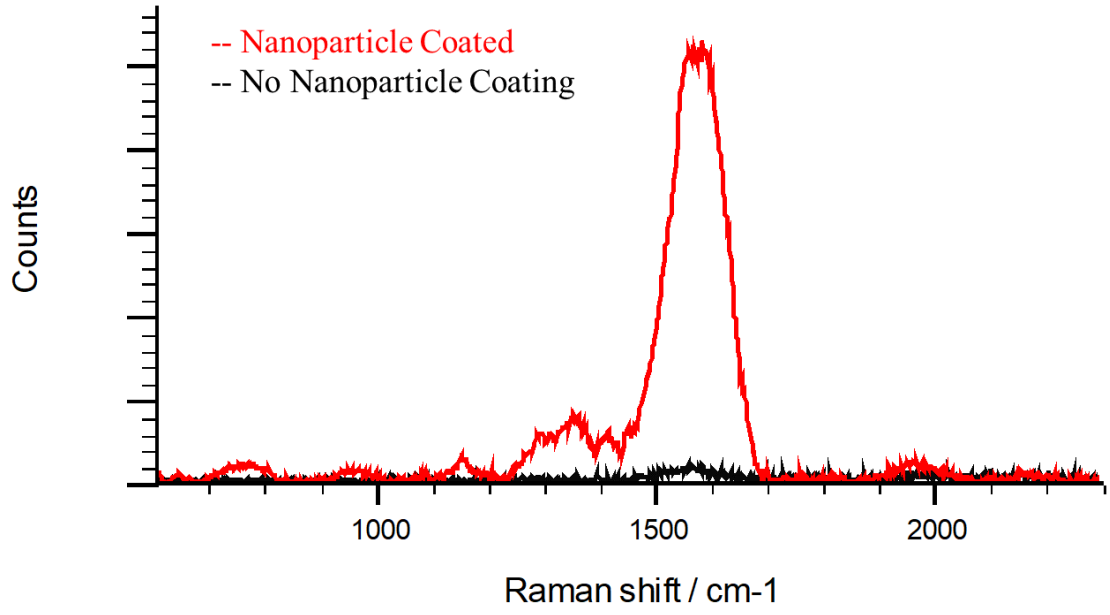

Figure 27: Raman spectra of DLC on a silver on silicon substrate with and without silver nanoparticle coatings.

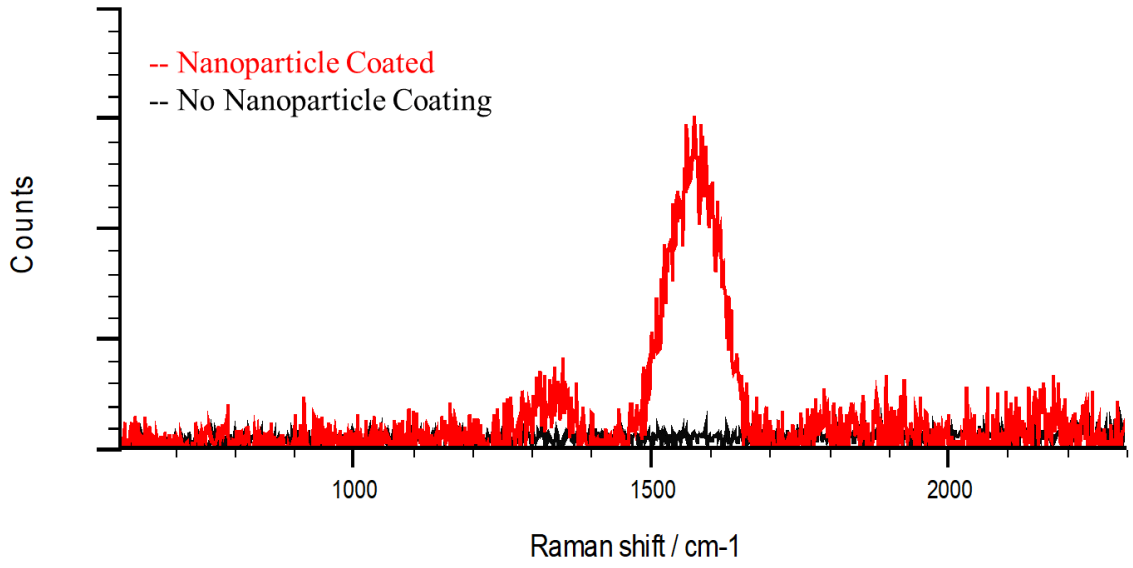

Figure 28: Raman spectra of DLC coated hard disk drive media with and without silver nanoparticle coatings.

A summary of the results for each type of sample can be seen in Table 1 below.

Table 1: SERS enhancement of various samples.

DLC Substrate	Nanoparticle Coated	No Nanoparticle Coating
Silicon	Enhancement Not Significant	Enhancement Not Significant
Ag Coated Silicon	Strong Enhancement	Enhancement Not Significant
Black Silicon	Enhancement Not Significant	Enhancement Not Significant
Ag Coated Black Silicon	Enhancement Not Significant	Enhancement Not Significant
Hard Disk Drive	Strong Enhancement	Enhancement Not Significant

3.2.4. Conclusions

The results from the SERS experiments show that it is possible to obtain plasmonically enhanced Raman scattering of DLC by placing plasmonic nanostructures above the DLC. This is important to the next experiment involving tip enhanced Raman spectroscopy (TERS) because TERS will operate by a plasmonic nanostructure above the analyte in order to create an enhanced electromagnetic field.

It is hypothesized that strong enhancement of the Raman scattering occurred on the silver coated silicon substrate with the silver nanoparticle coating due to a gap mode between the nanoparticles and the silver substrate. This is similar to a double-resonance SERS substrate [25]. The DLC coated sample with the silver coated silicon substrate, but without the silver nanoparticle coating, did not show significant enhancement possibly due to the lack of a gap mode.

It is also hypothesized that the hard disk drive media also exhibited a gap mode. Hard disk drive media may contain thin films of platinum group metals [26]. Platinum group metals are known to be plasmonically active and can exhibit a gap mode in proximity to a nanoparticle [27].

The black silicon samples did not show any enhancement, regardless of nanoparticle coating. It is theorized that the black silicon did not correctly form. Thus, no enhancement of the Raman scattering occurred.

4. Tip Enhanced Raman Spectroscopy

4.1. Introduction

While surface enhanced Raman spectroscopy does not provide localized electromagnetic field enhancement, tip enhanced Raman spectroscopy does (TERS). TERS can confine the enhanced electromagnetic field to nanoscale dimensions similar to that found in heat assisted magnetic recording drives (HAMR). Furthermore, TERS can produce a “lightning rod” electromagnetic enhancement effect [28] which is also used in HAMR nearfield transducers [29]. These aspects allow for better reproduction of electromagnetic radiation similar to that found in HAMR drives.

The goal of our TERS experiment is to use TERS to generate a localized enhanced electromagnetic field similar to that found in a HAMR while being able to simultaneously measure the Raman spectra. Yue et al. have already used a TERS instrument to simultaneously heat a silicon sample to above 200°C while simultaneously measuring the sample’s Raman spectra [30]. Our experiment differs in the fact that we used a more challenging thin film DLC sample and in the fact that we intend on heating the sample to much higher temperatures similar to that found in HAMR drives.

4.2. Principles of Tip Enhanced Raman Spectroscopy

Tip enhanced Raman spectroscopy uses localized surface plasmon resonance to increase the electromagnetic field strength of the probing laser of a Raman spectrometer [31]. In this way, TERS is very similar to surface enhanced Raman spectroscopy (SERS). In fact, TERS was original envisioned as a single particle SERS method. In TERS,

localize surface plasmon polaritons are created on the tip of a metal or metallized probe by the excitation laser of the Raman spectrometer. This generates a confined, i.e. nanofocused, electromagnetic field. Raman active molecules in close proximity to the tip exhibit enhanced Raman scattering in a similar phenomenon as that seen in nanostructure-based SERS. The probe can be scanned along a surface in order to generate a multi-dimensional map of Raman spectra [32]. Additionally, the metallic probe can enhance the electromagnetic field in the nearfield through a “lightning rod” type gap mode [33] similar to the gap mode in SERS.

4.3. Construction of TERS Setup

4.3.1. Integration of an Atomic Force Microscope with a Raman Spectrometer.

Initial efforts with regards to tip enhanced Raman spectroscopy were focused on modifying an existing commercial Raman spectrometer to conduct tip enhanced Raman spectroscopy experiments. These efforts were focused towards optically integrating a commercial atomic force microscope (AFM) with the Raman spectrometer. This involved designing an optical path from the spectrometer to the stage of an atomic force microscope using a system of adjustable mirrors as seen in Figure 29 below.

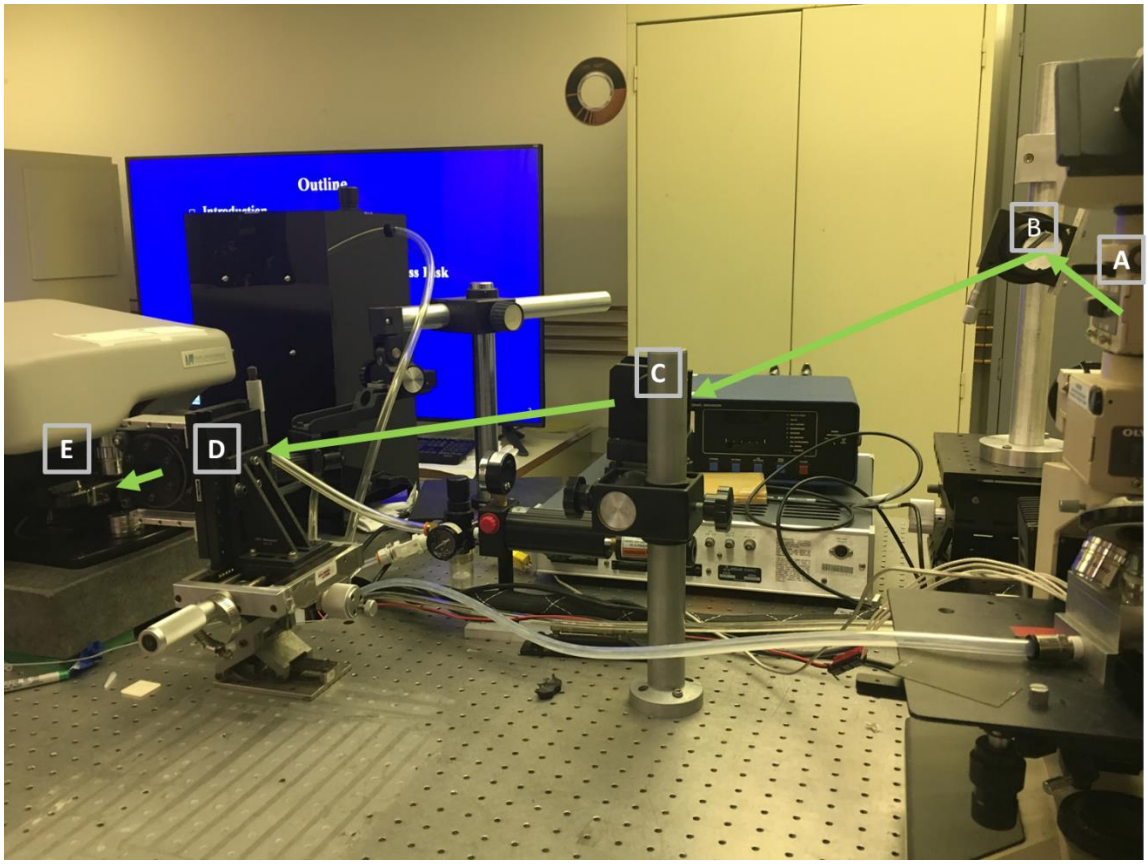

Figure 29: Optical path of tip enhanced Raman spectroscopy. The laser travels from Raman spectrometer (A) to the first mirror (B), second mirror (C), objective assembly (D), and atomic force microscope (E). Laser beam illustrated as green arrow.

The first task was to allow the excitation laser to exit the housing Raman spectrometer and to allow the Raman scattering to be collected through the same optical path as the exiting laser. This was achieved by adding a custom mirror to the microscope attached to the Raman spectrometer. The original and replacement parts can be seen in Figure 30 below. The replacement part functions by using a mirror to direct the excitation laser beam out of the back body of the microscope, bypassing the spectrometer's own microscope's optics, and then to the custom optical path seen in Figure 29. Returning Raman scattered light travels back to the spectrometer through the same optical path and

mirror system that is used to direct the excitation laser. The Raman scattered light will hit the mirrors and enter through a lowpass filter to the grating spectrometer system that is part of the Raman spectrometer. This configuration is possible because the Raman spectrometer was designed as a confocal micro Raman spectrometer. The spectrometer was designed to excite Raman scattering and collect the scattering in a coaxial configuration.

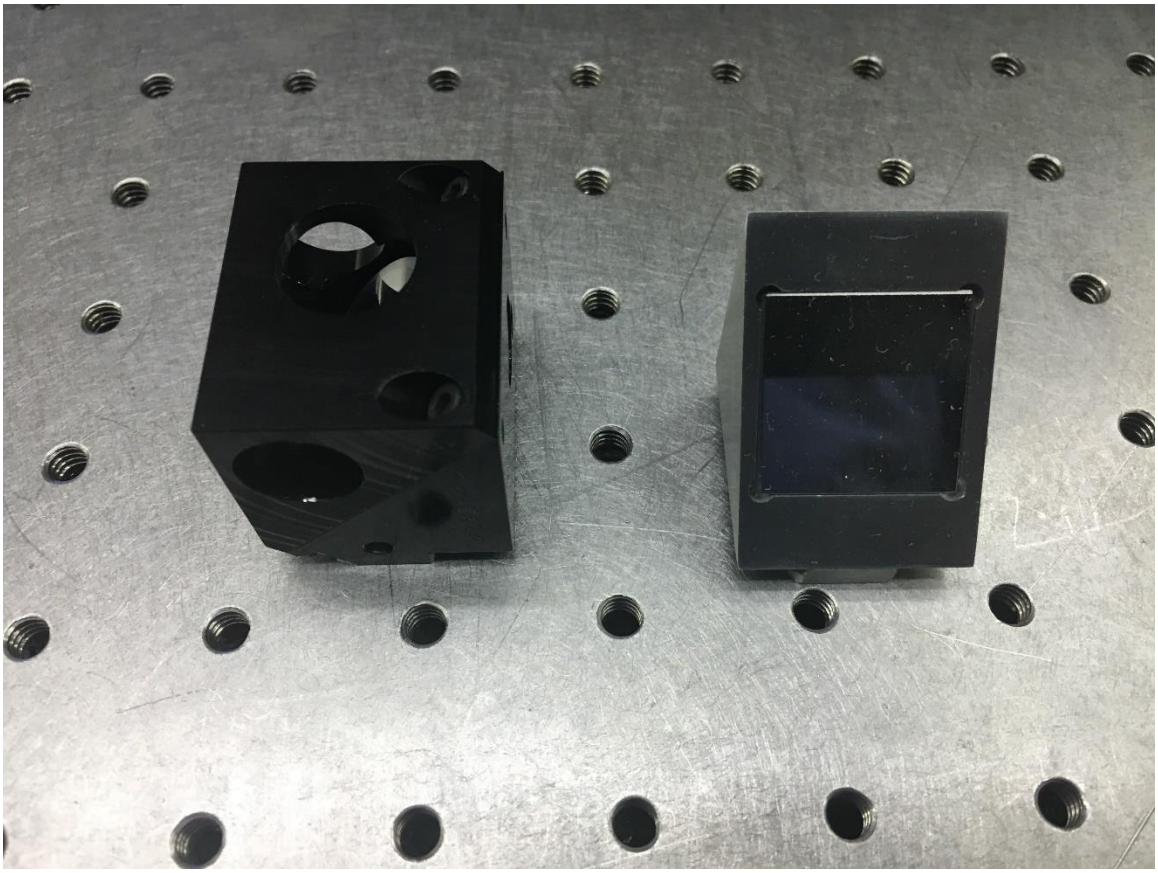

Figure 30: Original Raman spectrometer mirror (left) and custom designed replacement mirror (right).

Once the excitation laser exited the Raman spectrometer, it was directed to the AFM using a series of adjustable mirrors. The laser beam illuminated the AFM stage through a long working distance objective as seen in Figure 31 below. The objective

helped focus the laser and collect scattered light from the from the Raman scattering. The illumination was directed at a high angle of incidence, relative to the AFM stage surface, to clear the structure around the AFM probe holder.

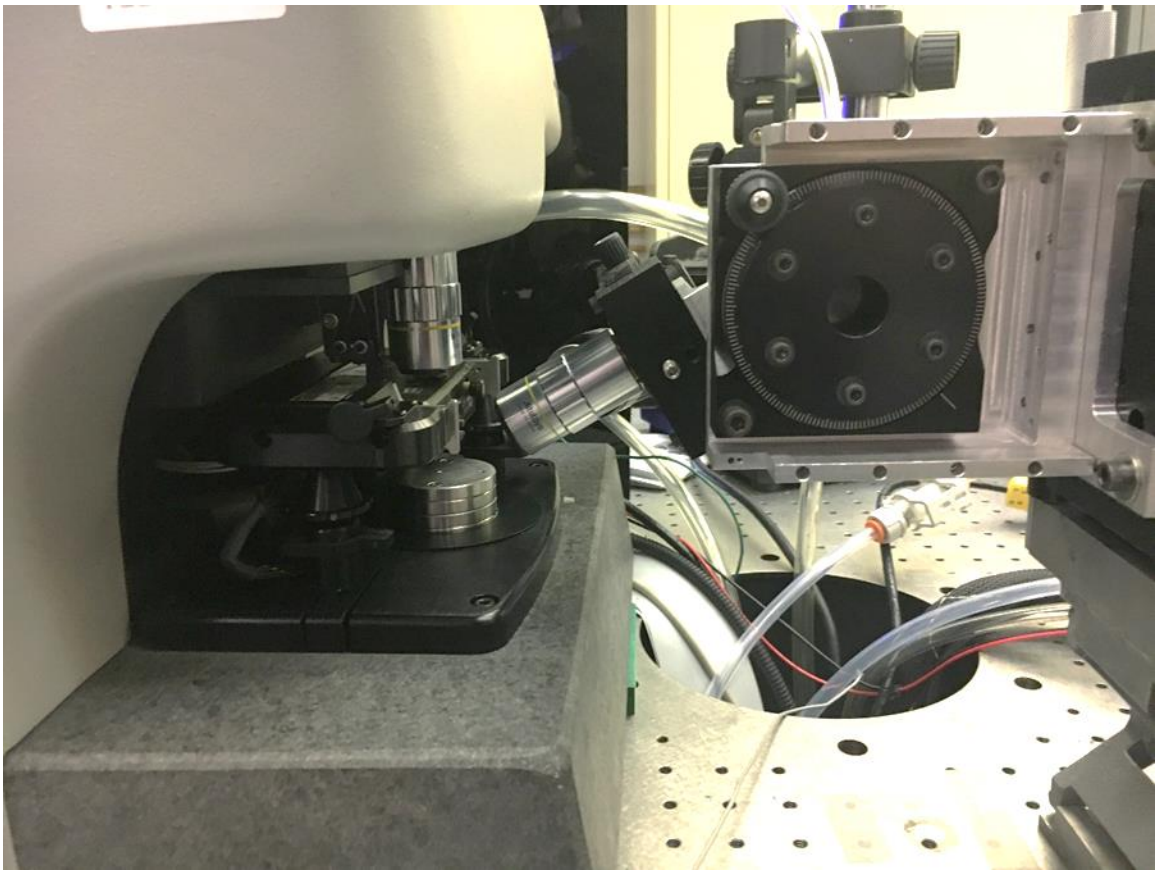

Figure 31: Objective assembly (right) and AFM stage (left).

With the optical setup, it was found that the collection efficiency of the system was not suitable for application to tip enhanced Raman microscopy. Loss of optical signal is thought to be originating from the limited optical access to the tip of the AFM probe where the Raman scattering should occur. Structures around the AFM scanning head obstructed the view of the AFM probe from many angles restricted the amount of scattered light that could be collected by the objective of the Raman spectrometer setup.

4.3.2. Construction of a Self-Actuating AFM

Without good optical access and a practical way to modify the AFM for optical access, it was decided that it would be best to manufacture a simplified version of a self-actuating AFM. This was a much lower risk than machining the AFM scanning apparatus, which contained delicate and costly piezoelectric actuators. Of the possible AFM designs available, a shear mode self-actuating design was chosen on the basis that the design had good optical access, was mechanically simple, and did not require a secondary laser which could interfere with the TERS measurement.

The self-actuating design that was chosen is based around the use of Bruker Nano Inc.'s tuning fork TERS-AFM probes. These probes were readily available for use and had verified performance on malachite green on gold test samples. The probe design is based off a vibrating quartz tuning fork which sweeps an electrochemically sharpened gold nanowire tip over the surface of interest. Changes in surface topography and other properties of the surface of interest can be determined by when the tip of the probe is placed in proximity to the surface and the surface forces become strong enough to influence the vibration of the quartz tuning fork. A diagram of the quartz tuning fork tip can be seen below in Figure 32.

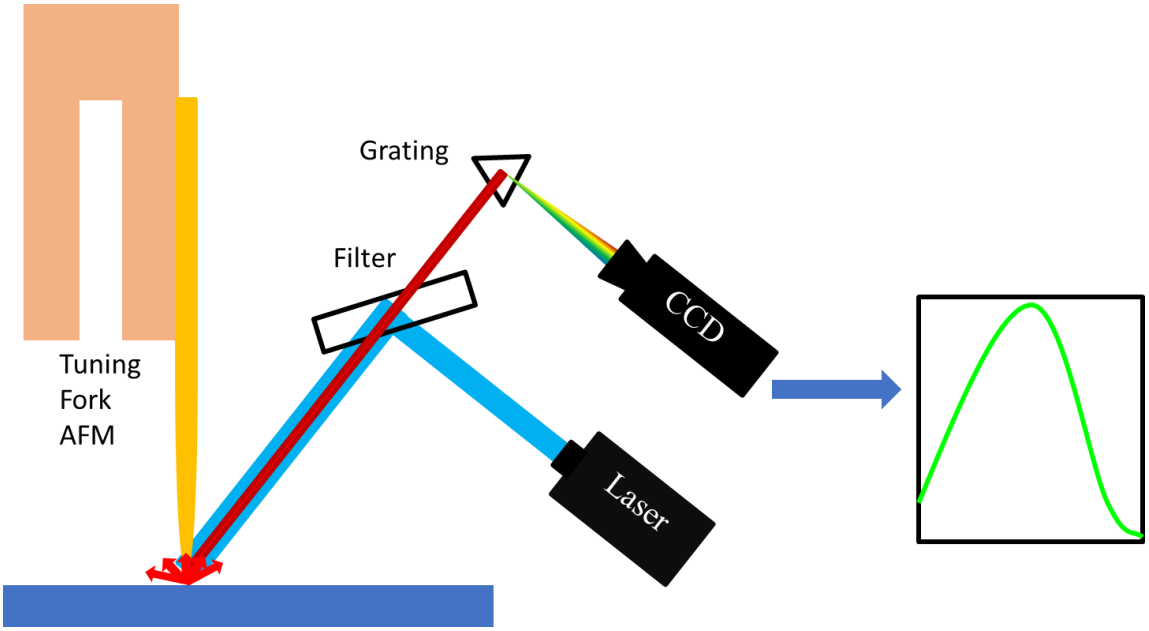

Figure 32: Schematic of a self-actuated tuning-fork based TERS spectrometer.

Electrical design and overall configuration of the system was roughly based off the concepts outlined in the papers by Otero [34] and by Ruiter [35]. A simplified version of the designs outlined in the papers was constructed. Excitation of the tuning fork and feedback would occur through a dual phase lock-in amplifier. Low noise amplifiers were placed in the circuit to amplify the signals into a range that is detectable by the data acquisition system. The lock-in amplifier was connected to a computer with a high-speed data acquisition system. Changes in the phase, frequency, bandwidth, or amplitude of the feedback signal can be determined by the computer. The computer processes the feedback signal and calculates an error signal with respect to a reference level. Then, the computer feeds the errors signal into a standard proportional-integral-derivative control loop and outputs a control signal to a piezoelectric actuator that adjusts the height of the tuning fork probe.

Mechanical design of the system was also simplified from the typical designs found in literature. The primary simplification is in the aspect that the design moves the tuning-fork AFM probe in a single dimension. A custom machined piece fitted with electrical contacts will hold the probe to a single dimension piezoelectric actuator. The piezoelectric actuator translates the AFM probe in the out-of-plane height direction. Rough translation for setup purposes is handled by a multi-axis micrometer stage. A diagram of the configuration can be seen in Figure 33 below.

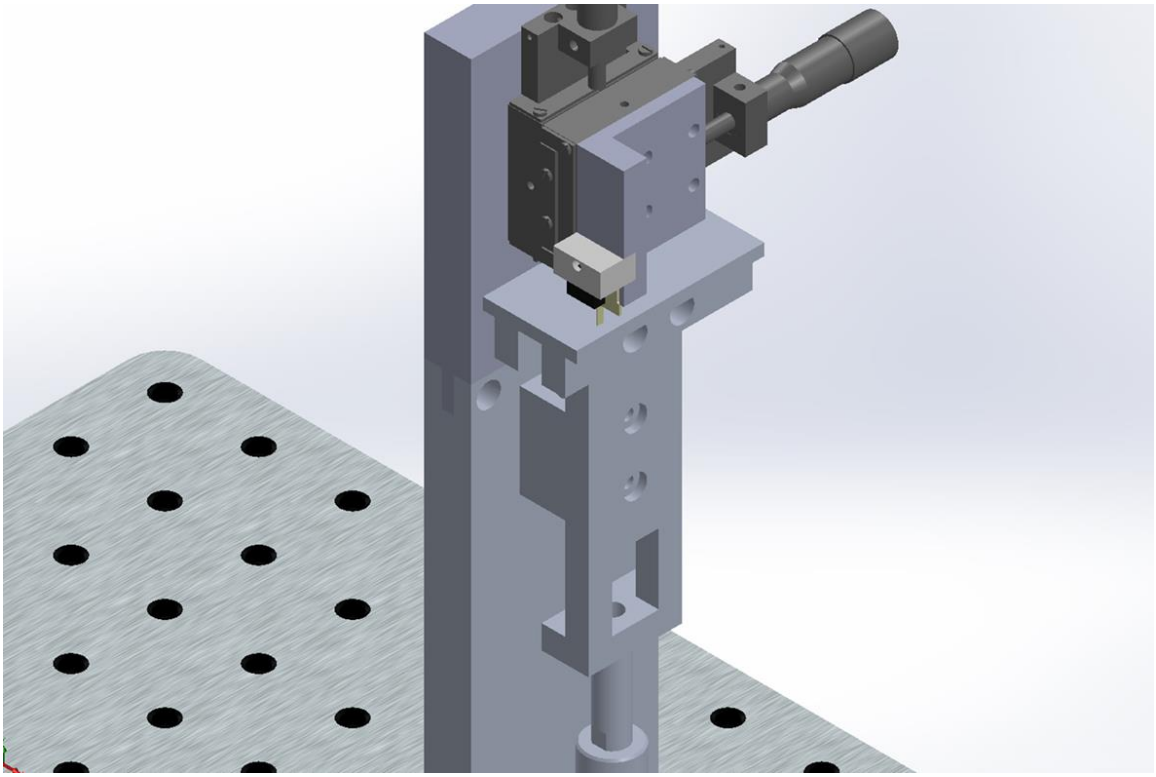

Figure 33: CAD model of tuning-fork based TERS system.

The simplified design was chosen on the basis that it would allow for greater optical access. Without the extra two dimensions of probe movement found in typical setups, the structure around the probe holder will be smaller and block less area. The

system will have two less piezoelectric actuators around the probe area. Additionally, the simplified design was faster to manufacture and deploy and required less electronics to control the position of the system.

The drawbacks of the system are that the setup was hard to align and tune. Optical alignment was achieved in the setup by manually adjusting the mirrors until one can see a peak in the amplitude of the Raman scattered light. Given that the mirrors were not designed for high precision aiming, the alignment procedure is extremely difficult due to the unsatisfactory precision of the mirrors in the optical path. Furthermore, tuning of the AFM control loop for the height of the tuning for AFM probe was also extremely difficult because the fine movement of the probe only occurs in a single dimension. Without the other dimensions, one could not use the typical 2-dimensional trace and retrace signals to tune the control loop. The lack of 3-dimensional scanning also prohibits one from checking the tuning of the AFM by imaging well defined structures. With these drawbacks in mind, and the fact that the tuning fork AFM tips are expensive and can be damaged by impacts from poor tuning, it was determined that a commercial TERS-AFM system would be better suited for the experiment.

4.4. Side-Illuminated Commercial TERS Setups

The side-illuminated commercial TERS setup that was used in the experiments was a Renishaw InVia Raman spectrometer mated to a Bruker Innova-Iris AFM. Another commercial system that was provided was a Renishaw InVia Raman spectrometer mated to a Nanonics SPM. Both commercial setups were similar to the initial setup in the sense

that they were created by mating a Raman spectrometer to an AFM. All of the setups were based off a Renishaw confocal micro Raman spectrometer. Light from the spectrometer is directed out of the spectrometer's microscope, reflected off guiding mirrors, and then focused onto the AFM stage with a long working distance objective. The instrument with Bruker Innova-Iris AFM was the setup that was primarily used for the following studies. An example of the setup from Renishaw can be seen in the Figure 34 below. As can be seen from the figure, the laser beam is guided through a closed beamline system that is mounted on a precision motorized positioning system. In addition, the system has an inline camera that allows for one to see their point of aim and for one to see the rough spacing and positioning of the AFM probe.

Figure 34: An example of a Bruker Innova-Iris AFM with a Renishaw Raman Spectrometer [36].

4.4.1. Use of Commercially Available Side-Illuminated TERS Probes

Initial experimentation was conducted with commercially available TERS probes. Of the multitude of TERS probes that are commercially available, Bruker's TERS-AFM tuning fork probes and Nanosensors' ATEC-CONTAu cantilever probes were selected. The Bruker tuning fork probes use a sharpened gold wire as the probe, while the Nanosensors probes are made from gold coated silicon. The Nanosensor probes were used in contact AFM mode.

4.4.2. Initial Experiments Using Commercial Tips and Side Illumination

Initial experiments ran during familiarization trials on the side-illuminated TERS setup showed that commercially purchased probes could produce enhanced Raman scattering. Although, several probes within the same batches did not produce enhanced Raman scattering. From SEM imaging, we suspect that the failed probes were either deformed from the factor or that the tuning fork mechanism failed to work, and the tip made hard contact with the surface. An example SEM image can be seen in Figure 35 below. This showed that the commercially purchased probes could be potentially unreliable for our application. For the initial experiments, a sample composed of malachite green coated on a gold substrate was used. In addition, a 633nm laser was used as the excitation light.

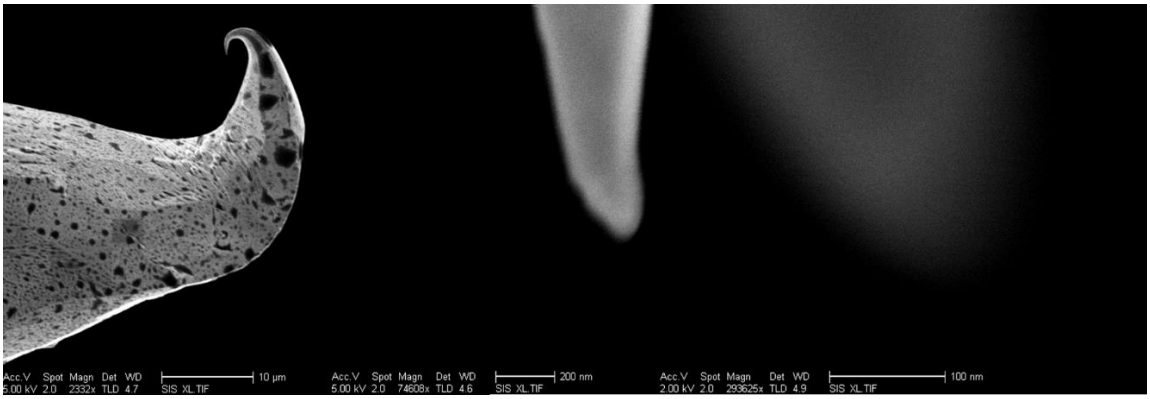

Figure 35: Sem images of a failed TERS tip from a commercial source.

Once working tips from a batch were identified, the malachite green sample was switched to a piece of diamond like carbon coated hard disk drive media, enhanced Raman scattering was not achievable using the side-illuminated TERS setup. Experiments using multiple excitation wavelengths were also conducted. They were also not able to produce enhanced Raman scattering. It was suspected that the malachite green coated gold sample produced an electromagnetic enhancement from an optimal gap mode and that the lack of enhanced Raman scattering from the hard disk drive media was from a lack of electromagnetic field enhancement. Another possibility was that the diamond like carbon does not have a large Raman cross section when using a 633nm laser as the excitation source. A 633nm laser was use due to the fact that the tips were designed to be used with a laser at approximately that wavelength.

4.4.3. Optimization of TERS Probes

Two possible solutions were considered for the difficulties with creating enhanced Raman scattering on the hard disk drive media. One solution was to try an alternative

TERS probe to see if other designs would be more successful. Another solution would be to optimize a probe so that it would work at a different excitation wavelength. The first solution was initially attempted due to it being the more straightforward than the latter solution.

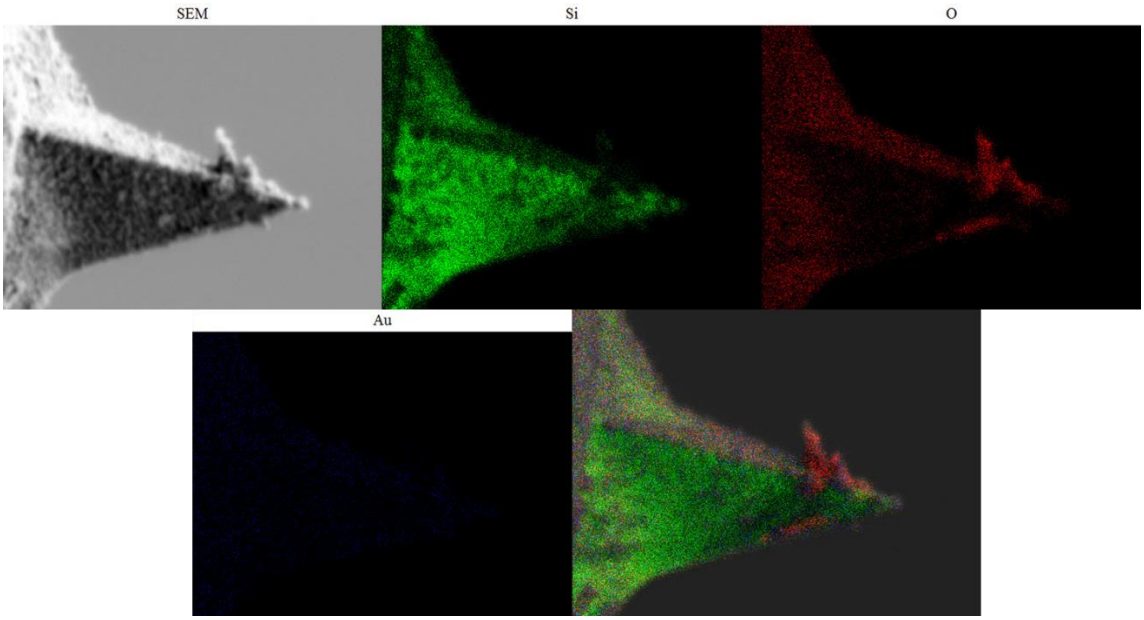

Figure 36: EDX maps of a gold coated AFM tip

Of the many different TERS probes described in the literature, the design by Hayazawa et al. was chosen for its straightforward design [37]. The design involved tools that were readily available to the laboratory. The manufacturing of the TERS probe involved creating an oxide layer by heating a Bruker OTESPA-R3 optical access AFM probe to 1000 degrees centigrade for 10 hours as described in the paper. After the oxide layer was created, gold was sputtered onto the AFM probe. Hayazawa's paper uses a process that evaporates silver onto the AFM probe after oxidation. Sputtering of gold was chosen because gold would not oxidize or tarnish in the time between the coating of the

TERS probe and the TERS experiment. In addition, sputter parameters were chosen so that a high-quality film would be form that would be like those deposited by evaporation. Successful deposition of the gold was visually verified. Energy dispersive x-ray spectroscopy (EDX) was used to image the gold coated tip. An example of an EDX map is show in Figure 36 above. EDX analysis had little utility due to the lack of signal due to the ultra-thin nature of the gold coating.

After manufacturing of the coated TERS probes, the probes were examined under light and electron microscopy. Optical analysis of the thin film interference within the oxide layer after the oxidation step allowed for the determination of the thickness of the oxide layer. An example of an oxidized tip can be seen in Figure 37 below. Scanning electron microcopy was used to determine the effect of the process on the geometry of the TERS probe.

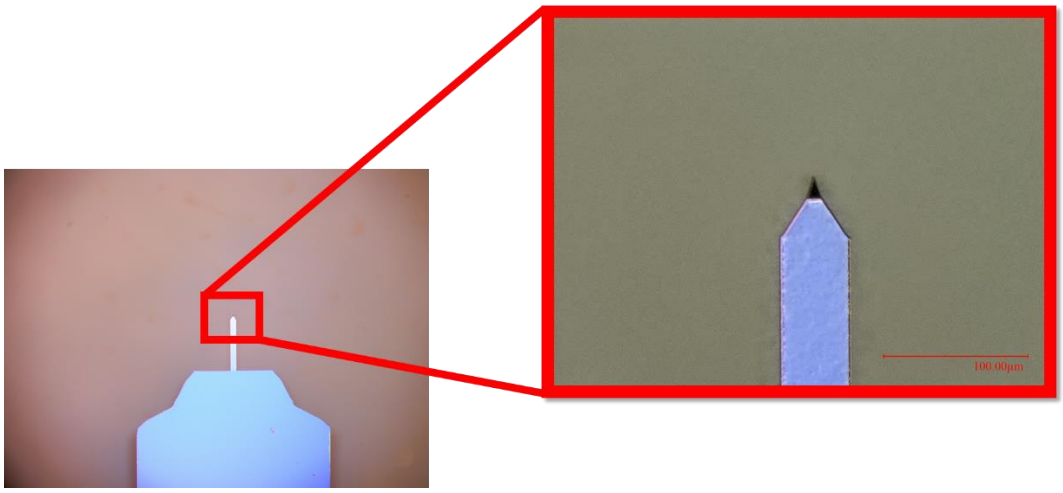

Figure 37: Image of an oxidized silicon AFM tip.

Scanning electron microscopy (SEM) showed that the TERS probe crated by the aforementioned process was too dull. The tip radius of the resulting probe was

approximately 500 nm. The SEM micrographs can be seen in Figure 38 below. Both the SEM micrographs and the optical analysis showed that the oxide layer was about 250 nm thick. Therefore, it is likely that the excessively thick oxide layer was causing the tip to be dulled. After this discovery, the oxidation process time was decreased in order to decrease the thickness of the oxidation layer. This was found to create unpredictable results in terms of oxide layer thickness. After these attempts, other probe designs were considered.

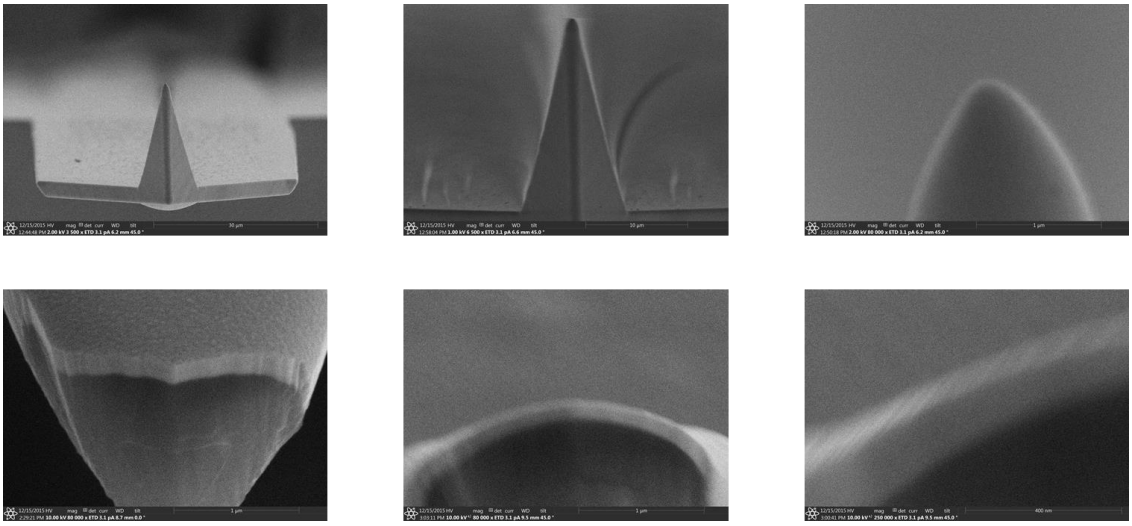

Figure 38: SEM micrographs of silicon AFM oxidized tips.

4.4.4. Potential Designs for TERS Probes

Several different TERS probe designs were considered many of which are outlined in the papers by Nononty et al. [38], by Zhang et al. [39], by Kharintsev et al. [40], by Berweger et al. [41], and by Maouli et al. [42]. The goal of the design was to create a tip that would enhance the near-field radiation between the probe and the sample surface using an optical antenna effect while operating at an excitation frequency that would

create maximal Raman scattering. In addition, it is preferable if the tip could be made out of a stable metal such as gold that would not degrade over time.

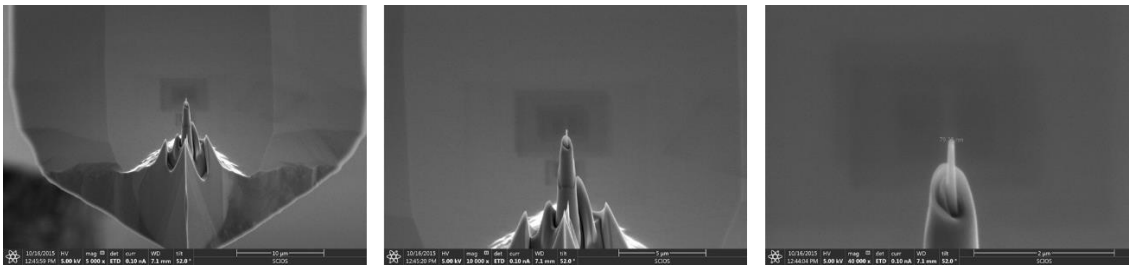

Figure 39: SEM micrograph of FIB sharpened platinum tipped TERS probe.

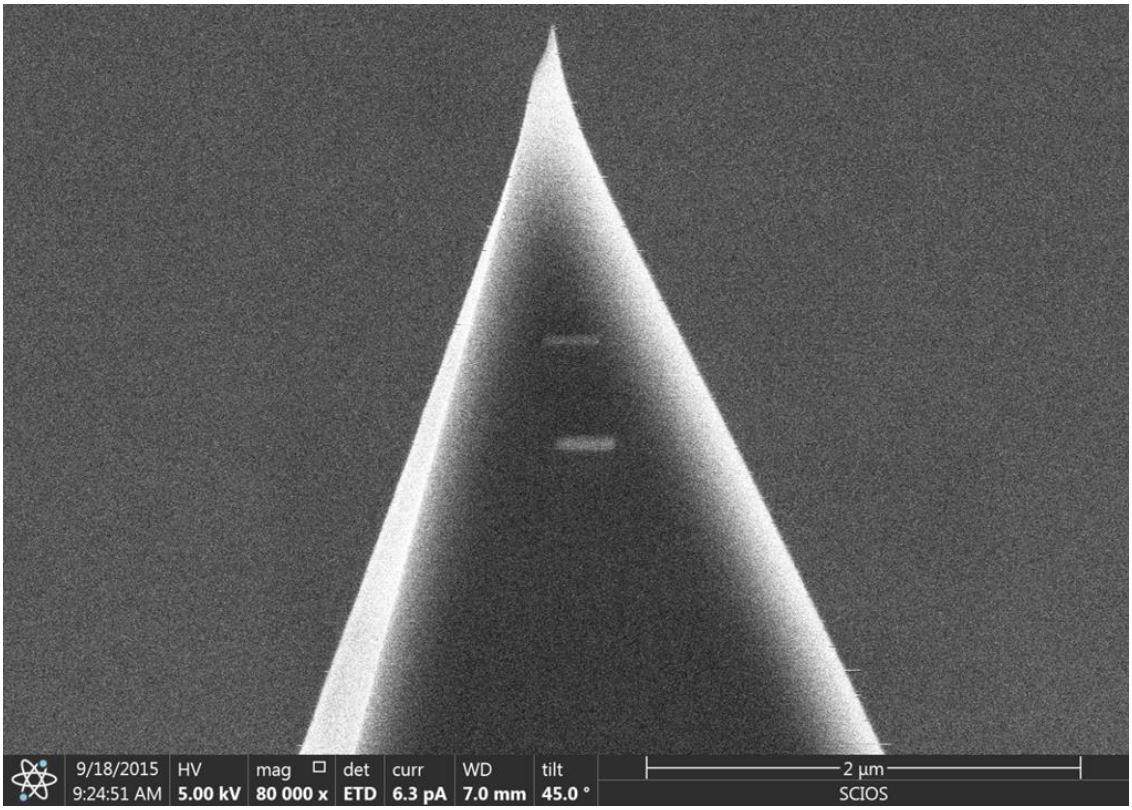

Figure 40: SEM micrograph of a nanoantenna TERS tip.

Two novel designs were created inspired by Maouli et al. modification of probe geometry using a focused ion beam (FIB) instrument and inspired by Curto et al. [43] and

Pavlov et al.'s [44] work with nanoantennae. The first design was constructed by depositing platinum on the apex of an AFM tip using electron-beam induced deposition (EBID). The apex was then sharpened using FIB. The second design involved depositing a resonant nanoantenna using platinum EBID. Both designs were manufactured using an FEI Scios dual beam FIB/SEM. Scanning electron microscope (SEM) micrographs of the FIB sharpened tip can be seen in Figure 39 above, and a SEM micrograph of the nanoantenna can be seen in Figure 40 above. CST Microwave Studio was used for the initial simulation of the nanoantenna probe, an example can be seen in Figure 41 below.

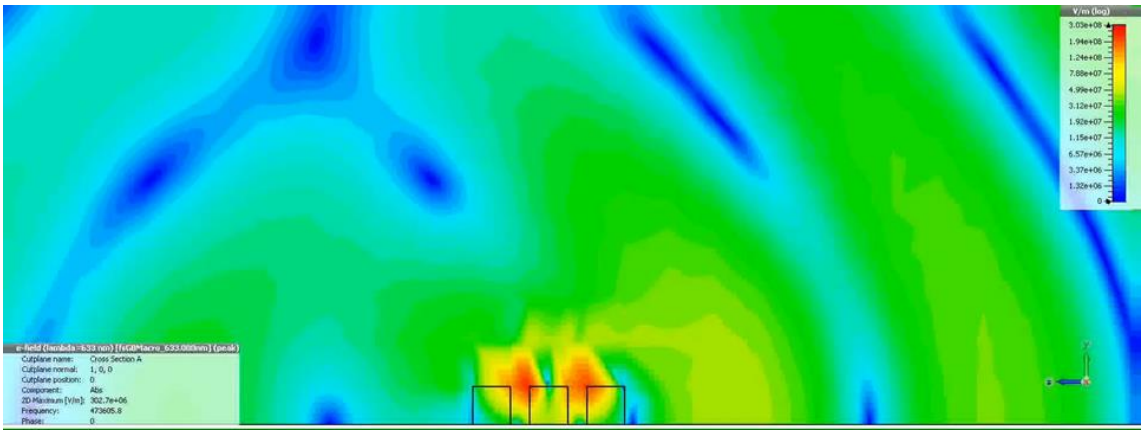

Figure 41: Simulation results from a nanoantenna design.

Upon qualitative EDX analysis of both probes, it was discovered that EBID created large amounts of residual carbon deposition due to the fact that the EBID process was using organometallic precursors. Due to the fact that the excess carbon has the potential to bias our TERS results, it was decided that another approach would be more feasible.

4.5. Top-Illuminated Commercial TERS Setups

4.5.1. Introduction

The probing and illumination methods for TERS setups vary greatly between different TERS instruments. The Bruker Innova-Iris AFM illuminates the probe tip from the side. A second TERS instrument that the author gained access to was a Nanonics SPM that illuminates the probe tip from the top side of the probe. Both illumination configurations have their benefits and limitations. For the side-illumined Bruker instrument, the scanner allows for the use of both a tuning fork type probe and cantilever-based probes. For the top-illumined Nanonics instrument, probes are limited to tuning fork type probes while the optics are more efficient at collecting Raman scattered light compared to the side-illumined setup.

4.5.2. Experimental Details

The Nanonics TERS SPM setup used a probe based off a nanopipette. The probe consists of a nanopipette with a gold nanosphere immobilized on the tip of the pipette. An SEM micrograph of a similar silver nanosphere probe from Nanonics can be seen in Figure 42 below. The instrument uses a 532nm laser for excitation. The Nanonics system also used a Renishaw Raman spectrometer to measure the Raman scattering. The same 20nm DLC on bare silicon and Showa Denko hard disk drive media as used in chapter 3 of this thesis was used as test samples.

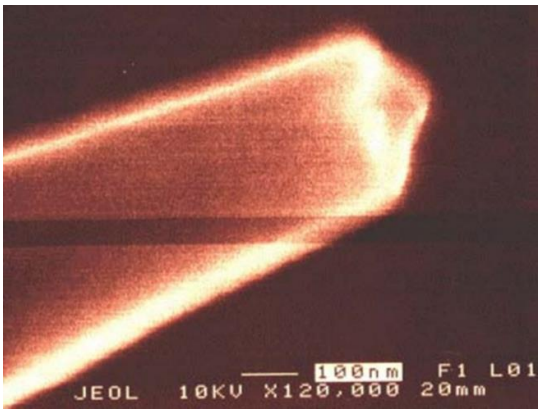

Figure 42: Example of a Nanonics apertureless TERS probe [45].

4.5.3. Results

Results showed that both the 20nm DLC sample and the hard disk drive media sample exhibited enhanced Raman scattering while being probed by the top-illuminated Nanonics TERS instrument. Both exhibit changes in the intensity ratio of the D to G peaks under near-field excitation. The hard disk drive media showed greater signal enhancement, as seen in Figure 43 (a)(b), compared to the 20nm DLC sample, as seen in Figure 43 (c)(d).

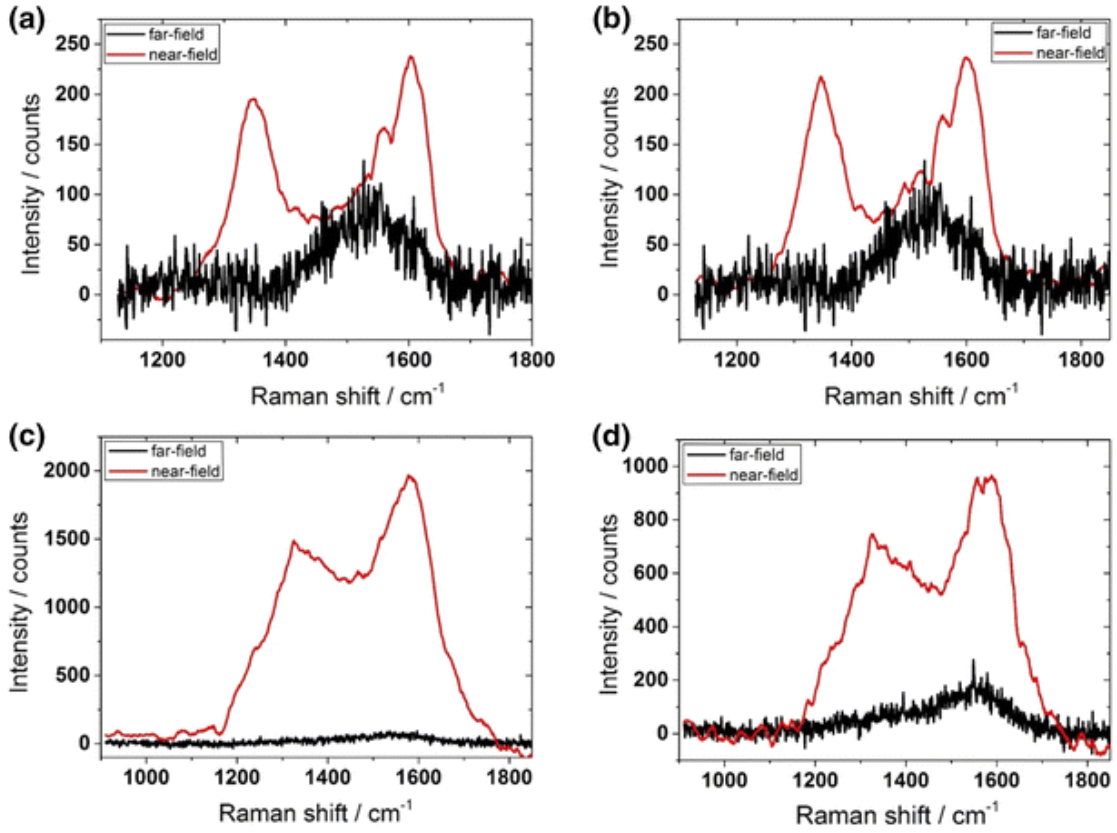

Figure 43: Raman spectra from tip-enhanced Raman scattering of 20nm DLC (a)(b) and of 3nm DLC from commercial hard disk media (c)(d). Previously published in [46].

4.5.4. Conclusions

A number of factors can possibly account for the differences in TERS signal enhancement between the 20nm DLC and the 3nm hard disk DLC samples. As mentioned before in chapter 3, the hard disk media may contain plasmonically active platinum group metals. This may create a gap mode [27] that further increases the electromagnetic field within the sample beyond that of the tip alone. Furthermore, differences in, the microstructure, topology, amorphicity, atomic bonding, and incidental contamination of the sample may influence the enhancement of the Raman spectra.

Additionally, the differences in the intensity ratio of the D to G peaks under near-field excitation when compared to the ratio under far field excitation may be due to local enhancement of inhomogeneous structures [47] and carbon chain configurations [48].

From this experiment, one can conclude that tip enhanced Raman spectroscopy is well suited for the study of the diamond like carbon overcoat on hard disk media. This is on the basis that TERS increases the signal to noise ratio of the Raman scattering by orders of magnitude. Furthermore, the TERS probe can be scanned across an area and allows one to map and visualize nanoscale phenomena occurring on the hard disk media. This is advantageous in studying heat assisted magnetic recording as damage occurs on the nanoscale.

5. Conclusion

5.1. Conclusions

Heat assisted magnetic recording drives (HAMR) are complex devices that rely on nanoscale phenomena in order to function. Engineers designing HAMR drives would greatly benefit from techniques that can provide insight into how HAMR drives wear in the nanoscale. Of primary concern is the nearfield optics, the heating and cooling cycle caused by the radiation from said optics, and the resulting damage cause by the intense thermal and electromagnetic cycling. Tip-enhanced Raman spectroscopy (TERS) offers a high-resolution technique for detecting and quantifying the nanoscale damage found in HAMR systems.

This thesis first examines changes the far-field Raman spectra of diamond like carbon (DLC) due to thermal cycling. It was found that G peak increased in wavenumber shift proportionally to an increase in the peak temperature in the thermal cycle when measured at room temperature after the thermal cycle has completed. It was also found that G peak decreases in wavenumber shift proportionally to an increase in the peak temperature in the thermal cycle when measured at the peak temperature during thermal cycling. Since the DLC is in a way a similar material to the DLC used in the carbon overcoat of hard disk drives, it was concluded that it may be possible to quantify wear in HAMR drives in terms of G-peak position versus thermal cycling parameters.

Since the thin film DLC in hard disk drives is on the order of nanometers in thickness, the far field Raman spectra of disk drive DLC exhibits poor signal to noise ratios due to the sheer lack of material that is required for Raman scattering. This limits

the amount and accuracy of data that one can ascertain from analyzing the Raman spectra. Thus, measurement of the Raman spectra of disk drive DLC using surface enhanced Raman spectroscopy (SERS) was perused. The SERS studies showed that SERS provides orders of magnitude more signal to noise ratio, as compared to far-field Raman, when measuring the Raman spectra of hard disk drive DLC. SERS additionally offers the benefit of using intense nearfield radiation, thereby opening up the possibility of using SERS to simulate the damaging electromagnetic conditions found in HAMR drives.

Tip-enhanced Raman spectroscopy further improves on SERS by localizing the near-filed plasmonic effects of SERS nanoparticles to the apex of a scanning probe. The TERS probe can be scanned across a sample, thus allowing for nanoscale mapping of the Raman spectra of a sample. Multiple commercial Raman instruments, commercial TERS probes, and novel self-made probes were experimented with in order to obtain a single-point TERS spectra on a DLC hard disk drive media sample. It was found that a top-illuminated Nanonics SPM, with a Renishaw Raman spectrometer, and with a Nanonics gold nanosphere TERS probe was the only setup that was able to conduct TERS on a DLC coated hard disk drive media sample. The collected TERS spectra also showed orders of magnitude greater signal to noise ratio compared to a far-field measurement. It was also observed that the nearfield TERS spectra had differences in peak amplitude ratios when compared to the peak amplitude ratios of the far field Raman spectra. This phenomenon seems to be well explained in the scientific literature.

Although an end goal of this study is to simultaneously generate HAMR-like radiation damage while measuring changes in the Raman spectra caused by said

radiation, this study did not progress to the point where the author was able to conduct the necessary experiments to do this. The author speculates that it is possible for one to simultaneously generate HAMR-like radiation damage while measuring changes in the Raman spectra by using TERS. Yanagisawa et al. have already used SERS to simultaneously generate HAMR-like radiation, measure temperature, and measure changes in the Raman spectra of lubricated hard disk drive DLC [49]. One can extend Yanagisawa's findings by using TERS instead of SERS. TERS has the advantage of creating a more highly localized electromagnetic field, more akin to that found in HAMR drives. In addition, one can map the effects of the nearfield radiation damage using TERS, at lower laser powers, after the damage has occurred.

The major challenge behind using TERS instead of SERS would be selecting or designing a TERS probe that could withstand the intense heat and electromagnetic radiation required to damage hard disk drive media. It is hypothesized that using a pulsed laser or using a plasmonically active refractory material such as platinum for the TERS probe may help reduce the thermal load on the tip.

5.2. Further Studies

Further studies include using the TERS system to generate Raman maps of various material used in the head/disk interface of hard disk drives. One can look for nanoscale damage or defects in the materials and correlate or find a causal relationship to changes in the Raman spectra. One can also intentionally cause electrical, laser, or mechanical damage and study their effects on the Raman spectra. A section of aluminum

titanium-carbide composite was extracted from the body of a hard disk drive slider using focused ion beam milling for the purpose of Raman spectroscopy mapping. One can use this sample to also see if TERS is suited for mapping nanoscale damage that occurs on hard disk drive sliders. The section can be seen in Figure 44 below

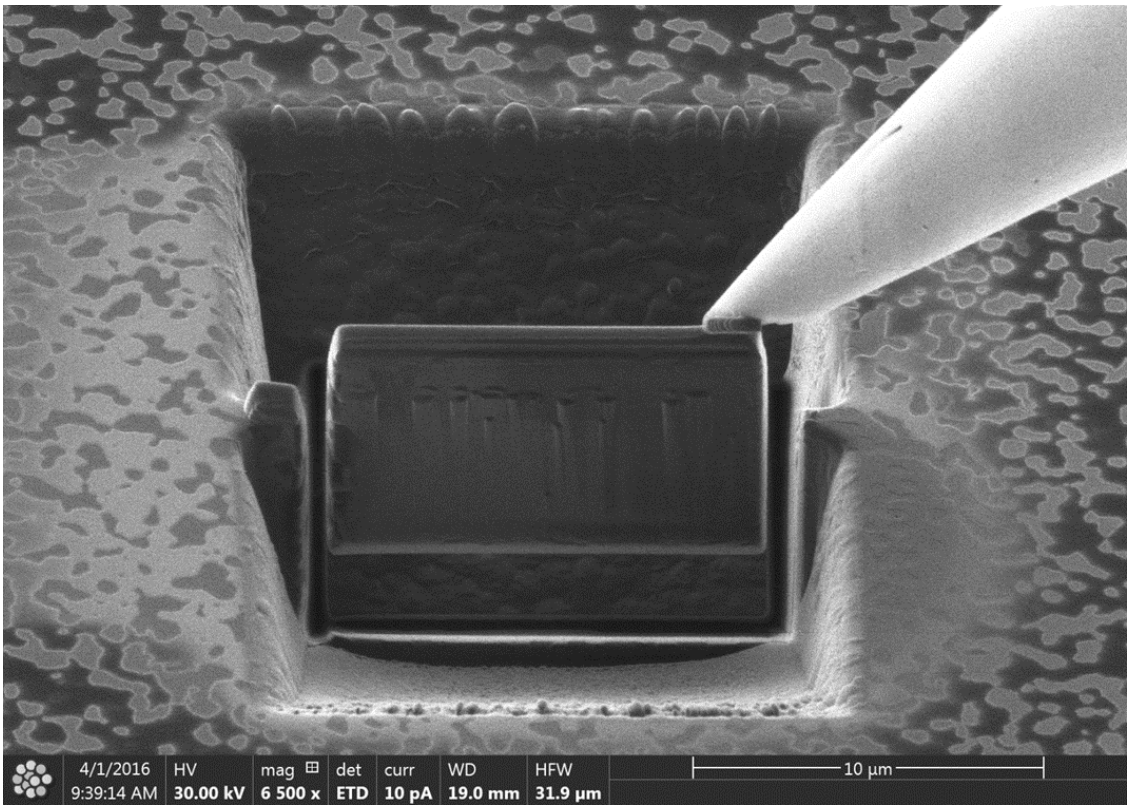

Figure 44: Section of aluminum titanium-carbide composite extracted from a hard disk drive slider.

Another possible study is to obtain HAMR heads and media, fly the head on the media using a spin stand, and attempt to measure the Raman scattering from the head disk interface. This would allow one to measure chemical changes in the head disk interface *in situ*. Possible challenges to this are that, Raman spectroscopy requires a relatively noise-free laser, the analytes may require the laser to be in a certain

polarization, there may be fluorescent materials in the area of interest, and there may not be sufficient optical access to the head/disk interface.

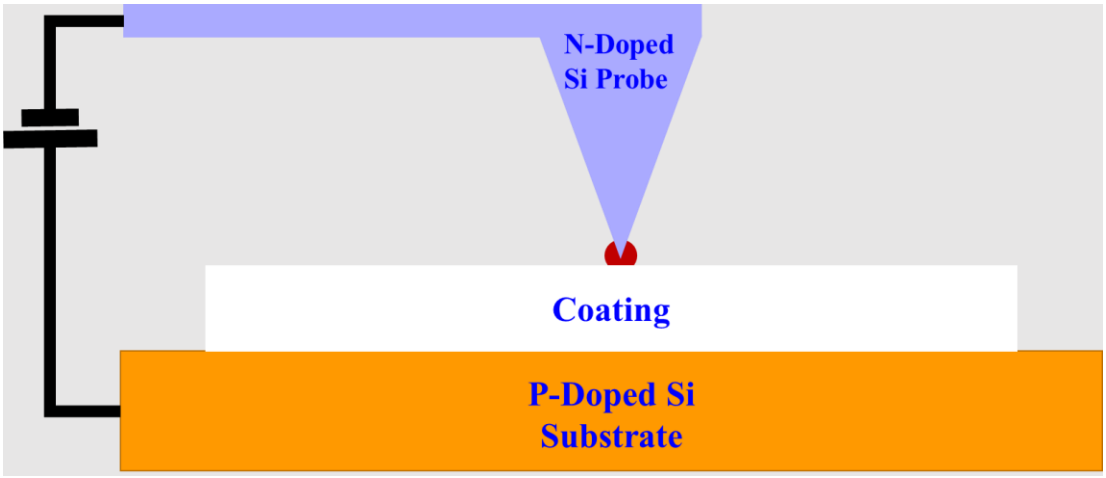

Figure 45: Diode junction formed by a p-doped silicon wafer and an n-doped AFM probe.

A potential study that is of scientific interest is to study the effects of an electric field on the Raman scattering of DLC. It is known that electric fields could affect the Raman scattering of a material [50]. Since the DLC is deposited on a p-doped silicon wafer, and it is easy to obtain n-doped silicon AFM tips, we can create a diode junction as seen in Figure 45 above. Initial experimentation has been conducted. Results can be seen in Figure 46 below. Although the results seem to suggest that the G peak of the Raman spectra is enhanced or suppressed as a function of bias voltage, the difference between the peaks lies within the error of the instrument. Thus, these results are inconclusive.

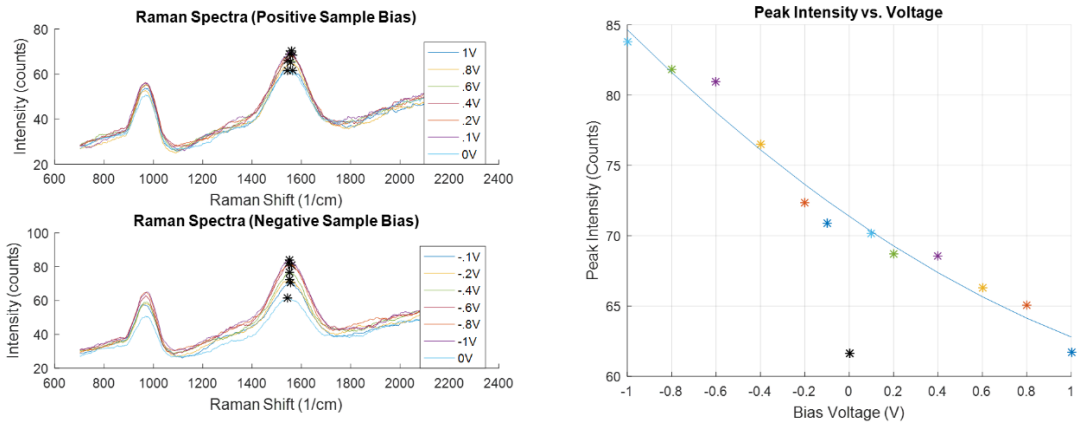

Figure 46: Results from Raman spectroscopy of a diode junction.

Bibliography

[1] Western Digital Corporation, "Western Digital 2016 Investor Day," 6 December 2016. [Online]. Available: http://files.shareholder.com/downloads/WDC/5336865652x0x920206/274557B2-F1B6-482E-B700-C8CBB0B6DF03/WDC_2016_Investor_Day_Presentations_12062016.pdf. [Accessed 2 October 2017].

[2] D. Reinsel, J. Gantz and J. Rydning, "Data Age 2025," November 2018. [Online]. Available: https://www.seagate.com/files/www-content/our-story/trends/files/idc-seagate-dataage-whitepaper.pdf. [Accessed 3 August 2019].

[3] M. Re, "Tech Talk on HDD Areal Density," 25 August 2015. [Online]. Available: http://www.seagate.com/www-content/investors/_shared/docs/tech-talk-mark-re-20150825.pdf. [Accessed 2 October 2017].

[4] Advanced Storage Technology Consortium, "2016 ASTC Technology Roadmap," 2016. [Online]. Available: http://idema.org/?page_id=5868. [Accessed 8 August 2019].

[5] H. Richter and S. Harkness., "Media for Magnetic Recording Beyond 100 Gbit/In.2.," *MRS Bulletin,* vol. 31, no. 5, p. 384–388, 2006.

[6] M. H. Kryder, E. C. Gage, T. W. McDaniel, W. A. Challener, R. E. Rottmayer, G. Ju, Y.-T. Hsia and M. F. Erden, "Heat Assisted Magnetic Recording," *Proceedings of the IEEE,* vol. 96, no. 11, pp. 1810-1835, 2008.

[7] L. Pan and D. B. Bogy, "Data Storage: Heat-Assisted Magnetic Recording," *Nature Photonics,* vol. 3, no. 40, pp. 189-190, 2009.

[8] J. R. Ferraro, K. Nakamoto and C. W. Brown, Introductory Raman Spectroscopy, 2 ed., San Diego: Academic Press, 2003.

[9] B&W Tek, "Theory of Raman Scattering," 2017. [Online]. Available: http://bwtek.com/raman-theory-of-raman-scattering/. [Accessed 30 11 2017].

[10] Nanophoton, "What is Raman Spectroscopy?," 2016. [Online]. Available: http://www.nanophoton.net/raman/raman-spectroscopy.html. [Accessed 3 12 2017].

[11] J. R. Serrano and T. E. Beechem, "Raman Thermometry of Microdevices: Comparing Methods to Minimize Error," *Spectroscopy,* vol. 26, no. 11, pp. 36-44, 2011.

[12] P. Kocevar, "Hot phonon dynamics," *Physica B+C,* vol. 134, no. 1-3, pp. 155-163, 1985.

[13] ASTM International, ASTM E2911-13 Standard Guide for Relative Intensity Correction of Raman Spectrometers, West Conshohocken, PA: ASTM International, 2013.

[14] J. F. Kielkopf, "New approximation to the Voigt function with applications to spectral-line profile analysis," *Journal of the Optical Society of America,* vol. 63, no. 8, pp. 987-995, 1973.

[15] J. B. Cui, K. Amtmann, J. Ristein and L. Ley, "Noncontact temperature measurements of diamond by Raman scattering spectroscopy.," *Journal of Applied Physics,* vol. 83, no. 12, pp. 7929-7933, 1998.

[16] A. C. Ferrari and J. Robertson, "Raman spectroscopy of amorphous, nanostructured, diamond–like carbon, and nanodiamond," *Philosophical Transactions of the Royal Society of London A: Mathematical, Physical and Engineering Sciences,* vol. 362, no. 1824, pp. 2477-2512, 2004.

[17] T. Beechem, S. Graham, S. P. Kearney, L. M. Phinney, Serrano and J. R., "Invited Article: Simultaneous mapping of temperature and stress in microdevices using micro-Raman spectroscopy.," *Review of Scientific Instruments* , vol. 78, no. 6, p. 061301, 2007.

[18] Technical University of Denmark, "Linkam heat/cool stage," 8 June 2017. [Online]. Available: https://www.kemi.dtu.dk/english/research/physicalchemistry/raman_spektroskopi/linkam-heatcool-stage. [Accessed 13 8 2018].

[19] L. Li, B. Suen and F. E. Talke, "Investigation of Temperature Dependence of Raman Shift of Diamond-Like Carbon Coatings Used in Heat-Assisted Magnetic Recording.".

[20] N. Wang, K. Komvopoulos, F. Rose and B. Marchon, "Structural stability of hydrogenated amorphous carbon overcoats used in heat-assisted magnetic recording investigated by rapid thermal annealing," *Journal of Applied Physics,* vol. 113, no. 8, p. 083517, 2013.

[21] E. C. Le Ru and P. G. Etchegoin, Principles of Surface-Enhanced Raman Spectroscopy, Amsterdam: Elsevier B.V., 2009.

[22] P. L. Stiles, J. A. Dieringer, N. C. Shah and R. P. V. Duyne, "Surface-Enhanced Raman Spectroscopy," *Annual Review of Analytical Chemistry,* vol. 1, pp. 601-626, 2008.

[23] A. C. Ferrari and J. Robertson, "Resonant Raman spectroscopy of disordered, amorphous, and diamondlike carbon," *PHYSICAL REVIEW B,* vol. 64, no. 7, p. 075414, 2001.

[24] Y.-L. Deng and Y.-J. Juang, "Black silicon SERS substrate: Effect of surface morphology on SERS detection and application of single algal cell analysis," *Biosensors and Bioelectronics,* vol. 53, no. 15, pp. 37-42, 2014.

[25] Y. Chu, M. G. Banaee and K. B. Crozier, "Double-Resonance Plasmon Substrates for Surface-Enhanced Raman Scattering with Enhancement at Excitation and Stokes Frequencies," *ACS Nano,* vol. 4, no. 5, pp. 2804-2810, 2010.

[26] B. Lu and D. Weller, "Chemically ordered, cobalt-three platinum alloys for magnetic recording". United States of America Patent 7,186,471, 6 March 2007.

[27] K. Ikeda, J. Sato and K. Uosaki, "Surface-enhanced Raman scattering at well-defined single crystalline faces of platinum-group metals induced by gap-mode plasmon excitation," *Journal of Photochemistry and Photobiology A: Chemistry,* vol. 221, no. 2-3, pp. 175-180, 2011.

[28] Z. Yang, J. Aizpurua and H. Xu, "Electromagnetic field enhancement in TERS configurations," *Journal of Raman Spectroscopy,* vol. 40, pp. 1343-1348, 2009.

[29] W. A. Challener, C. Peng, A. V. Itagi, D. Karns, W. Peng, Y. Peng, X. Yang, X. Zhu, N. J. Gokemeijer, Y.-T. Hsia, G. Ju, R. E. Rottmayer, M. A. Seigler and E. C. Gage, "Heat-assisted magnetic recording by a near-field transducer with efficient optical energy transfer," *Nature Photonics,* vol. 3, p. 220–224 , 2009.

[30] Y. Yue, X. Chen and X. Wang, "Noncontact Sub-10 nm Temperature Measurement in Near-Field Laser Heating," *ACS Nano,* vol. 5, no. 6, pp. 4466-4475, 2011.

[31] N. Kumar, S. Mignuzzi, W. Su and D. Roy, "Tip-enhanced Raman spectroscopy: principles and applications," *EPJ Techniques and Instrumentationvolume* , vol. 2, no. 9, 2019.

[32] P. Verma, "Tip-Enhanced Raman Spectroscopy: Technique and Recent Advances," *Chemical Reviews,* vol. 117, no. 9, pp. 6447-6466, 2017.

[33] W. Zhang, B. S. Yeo, T. Schmid and R. Zenobi, "Single Molecule Tip-Enhanced Raman Spectroscopy with Silver Tips," *The Journal of Physical Chemistry C,* vol. 111, no. 4, pp. 1733-1738, 2007.

[34] J. Otero, L. Gonzalez and M. Puig-Vidal, "Nanocharacterization of soft biological samples in shear mode with quartz tuning fork probes," *Sensors,* vol. 12, no. 4, pp. 4803-4819, 2012.

[35] A. Ruiter, K. Van Der Werf, J. Veerman, M. Garcia-Parajo, W. Rensen and N. Van Hulst, "Tuning fork shear-force feedback," *Ultramicroscopy,* vol. 71, no. 1, pp. 149-157, 1998.

[36] Renishaw PLC, "Raman-SPM/AFM combined systems," 2019. [Online]. Available: https://www.renishaw.com/en/raman-spm-afm-combined-systems--6638. [Accessed 25 July 2019].

[37] N. Hayazawa, T. Yano and K. Satoshi, "Highly Reproducible Tip-Enhanced Raman Scattering Using an Oxidized and Metallized Silicon Cantilever Tip as a Tool for Everyone," *Raman Spectroscopy,* vol. 43, no. 9, pp. 1177-1182, 2012.

[38] L. Novotny and N. Van Hulst, "Antennas for Light," *Nature Photonics,* vol. 5, no. 2, pp. 83-90, 2011.

[39] Z. Zhang, P. Ahn, B. Dong, O. Balogun and C. Sun, "Quantitative Imaging of Rapidly Decaying Evanescent Fields Using Plasmonic Near-Field Scanning Optical Microscopy," *Scientific Reports,* vol. 3, 2013.

[40] S. S. Kharintsev, G. G. Hoffmann, A. I. Fishman and M. K. Salakhov, "Plasmonic optical antenna design for performing tip-enhanced Raman spectroscopy and microscopy.," *Journal of Physics D: Applied Physics,* vol. 46, no. 14, p. 145501, 2013.

[41] S. Berweger, J. M. Atkin, R. L. Olmon and M. B. Raschke, "Light on the Tip of a Needle: Plasmonic Nanofocusing for Spectroscopy on the Nanoscale," *Physical Chemistry Letters,* vol. 3, no. 7, pp. 945-952, 2012.

[42] I. Maouli, A. Taguchi, Y. Saito, S. Kawata and P. Verma, "Optical antennas for tunable enhancement in tip-enhanced Raman spectroscopy imaging," *Applied Physics Express,* vol. 8, no. 3, p. 032401, 2015.

[43] A. G. Curto, G. Volpe, T. H. Taminiau, M. P. Kreuzer, R. Quidant and N. F. v. Hulst, "Unidirectional Emission of a Quantum Dot Coupled to a Nanoantenna," *Science,* vol. 329, no. 5994, pp. 930-933, 2010.

[44] R. S. Pavlova, A. G. Curto and N. F. v. Hulst, "Log-periodic optical antennas with broadband directivity," *Optics Communications,* vol. 285, no. 16, pp. 3334-3340, 2012.

[45] Nanonics Imaging Ltd., "Apertureless Probes," [Online]. Available: http://www.nanonics.co.il/products/apertureless-probes. [Accessed 11 7 2019].

[46] R. Andreas, L. Freeman, B. Suen, Y. Fainman and F. E. Talke, "Tip-Enhanced Raman Spectroscopy Studies on Amorphous Carbon Films and Carbon Overcoats in Commercial Hard Disk Drives," *Tribology Letters,* vol. 66, no. 54, 2018.

[47] M. Veres, M. Füle, S. Tóth, M. Koós and I. Pócsik, "Surface enhanced Raman scattering (SERS) investigation of amorphous carbon," *Diamond and Related Materials,* vol. 13, no. 4-8, pp. 1412-1415, 2004.

[48] A. Kudelski and B. Pettinger, "SERS on carbon chain segments: monitoring locally surface chemistry," *Chemical Physics Letters,* vol. 321, no. 5-6, pp. 356-362, 2000.

[49] M. Yanagisawa, M. Kunimoto, M. Saito and T. Homma, "HAMR Emulation Using Plasmonic SERS Sensor As Near Field Transducer," in *ASME-JSME 2018 Joint International Conference on Information Storage and Processing Systems and Micromechatronics for Information and Precision Equipment*, San Francisco, 2018.

[50] F. Schäffler and G. Abstreiter, "Electric-field-induced Raman scattering: Resonance, temperature, and screening effects," *Physical Review B,* vol. 34, no. 6, pp. 4017-4075, 1986.